Numerical investigation of highly excited magnetic monopoles in $SU(2)$ Yang-Mills-Higgs theory

Gyula Fodor* and István Rácz†

MTA RMKI, H-1525 Budapest 114, P.O. Box 49, Hungary

(Received 30 August 2007; published 18 January 2008)

Preliminary results concerning the time evolution of strongly exited $SU(2)$ Bogomolny-Prasad-Sommerfield (BPS) magnetic monopoles have been published in G. Fodor and I. Rácz, Phys. Rev. Lett. **92**, 151801 (2004). The behavior of these dynamical magnetic monopoles was investigated by means of numerical simulations in the four-dimensional Minkowski spacetime. The developed code—although applied to spherically symmetric configurations—incorporates both the techniques of conformal compactification and that of the hyperboloidal initial value problem. Our primary aim here is to provide a detailed account on the methods and results of the investigations reported in G. Fodor and I. Rácz, Phys. Rev. Lett. **92**, 151801 (2004). In addition, some important new results, which go much beyond the scope of these early studies, are also presented. In particular, to be able to distinguish linear and nonlinear effects, evolutions of monopoles deformed by various excitations, including both very small and extra large energy excitation, are investigated. In addition, a detailed account is provided on the spacetime dependence of the basic variables, as well as that of the other physically significant dynamical qualities such as the energy and energy current densities, the radial and angular pressures, and the magnetic charge density. A careful comprehensive study of the associated energy transfers and energy balances is also included.

DOI: 10.1103/PhysRevD.77.025019 PACS numbers: 03.50.Kk, 14.80.Hv

I. INTRODUCTION

Soliton and quasisoliton type configurations, which are in general spatially localized nonsingular finite energy solutions of nonlinear field equations, play a significant role in various particle physics considerations (see e.g. [1,2] for recent reviews). In general the associated field equations are highly nonlinear, therefore, most of the investigations have been restricted to the study of time-independent configurations. Thereby, there is an obvious increase of interest to study the dynamical properties of soliton type configurations. It is a matter of fact that the available analytic techniques either have not been developed enough to provide or simply cannot guarantee completely satisfactory answers to all questions in the case of nonlinear systems. Therefore, reliable numerical approaches are needed which are able to describe the time evolution of these type of systems. Motivated by these sorts of necessities, we have developed a numerical method which has been used in studying the time evolution of various spherically symmetric nonlinear dynamical systems [3–6] (see also [7–10]). The numerical approach we applied is based on the ''method of lines'' in a fourth order setting [11] which was found to be the most efficient among the numerical methods which are applied in various considerations [12]. In addition, to get a faithful representation of all the radiation processes, the techniques of conformal compactification (introduced first by Penrose [13]) to the underlying Minkowski spacetime, along with the hyperboloidal initial value problem were incorporated. The applied conformal gauge, which is a modification of the static hyperboloidal gauge, makes it possible to investigate by numerical means the asymptotic properties of radiation processes. One of the associated advantages is that by making use of this method, the radiation processes, which last infinitely long in physical time, can be analyzed in finite computational time intervals.

Among the great variety of physically interesting soliton type configurations, distinguished attention has been paid to the study of magnetic monopole type configurations such as the 't Hooft-Polyakov magnetic monopole solutions of coupled Yang-Mills–Higgs (YMH) systems [14]. However, even in the case of magnetic monopoles there was a lack of knowledge concerning the dynamical properties of these systems. Therefore, our numerical method was first applied to the study of the dynamical properties of the simplest possible magnetic monopole system, which could be chosen so that there was a radiative component among the basic field variables. This paper is, in fact, to report about the results of investigations concerning the time evolution of a strongly excited spherically symmetric $SU(2)$ BPS magnetic monopole [15].

To have a clear enough setting, at least from an ''energetic'' point of view, we investigated the time evolution of an initially static $SU(2)$ BPS magnetic monopole which was excited by the help of a high energy pulse. The self-interaction of the Higgs field was turned off which yielded a Yang-Mills–Higgs system so that the Yang-Mills field is massive while the Higgs field is massless.

The dynamics started by injecting a pulse of excitation via the time derivative of the Yang-Mills variable. Since the Yang-Mills and Higgs variables are coupled (in a nonlinear manner) energy was transformed to the massless

*gfodor@rmki.kfki.hu
†iracz@sunserv.kfki.hu

Higgs field which immediately forwarded *about half* of the energy of the pulse towards future null infinity, $\mathscr{I}^+$. It is already a surprise that this reaction of the monopole is apparently independent of the energy content of the exciting pulse, at least in the case of the subclass considered in this paper (see Sec. VII B 2). Nevertheless, naively, one might still expect that the following part of the evolution is going to be quite boring since only a lower scale energy transform will happen until the rest of the energy of the exciting pulse disperses and the system settles down to the static monopole.

Contrary to this simple hypothetical scenario, quite interesting features of the underlying nonlinear system show up. First, it was found that the exciting pulse leaves the central region so that it drags some part of the energy of the original static monopole with itself. This process is justified by the fact that in the central region, where a long-lasting quasistable ''breathing state'' develops, at least at the beginning of the evolution the average energy density is always less than the static monopole was. Since the original static magnetic monopole is stable we know that by the end the missing energy has to come back to the central region. However, as our numerical simulations indicates [5] this process is unexpectedly slow and, in certain cases, behaves completely contrary to our expectations. For instance, the difference between the dynamical and the original static energies contained in a ball of radius r may be positive or negative depending on the strength of the nonlinear aspects of the dynamics, as well as, on location, i.e. on the value of r. In particular, the time dependence of this ''extra energy'' content can be characterized by its high frequency oscillating part and by its mean value. We found a ''universal'' time decay for the amplitude of the high frequency oscillations of the form of a power law with exponent close to the ''ideal'' value $-5/6$. However, the exponent of the similar power law time decay of the mean value varies with the radius of the ball (see Sec. VII C 5).

It is also a characteristic feature of the evolution that some part of the energy of the exciting pulse is getting to be stored by expanding shells of oscillations of the massive Yang-Mills field built up in the distant region. These shells of oscillations behave much like the oscillations of a simple massive Klein-Gordon field (see [4] for a detailed investigation) since the coupling of the Yang-Mills and Higgs variables is negligible there. The monopole can pull back the missing energy, approaching the static configuration in the central region, only before these shells get too far away.

Because of the coupling of the Yang-Mills and Higgs fields in the central region, along with the ''breathing'' of the monopole there, the massless Higgs field continuously takes away a small fragment of the energy of the monopole, which is radiated to future null infinity. The corresponding decrease of the total energy which can be associated with the hyperboloidal hypersurfaces decreases in time with power $-2/3$ (see Sec. VII C 4). Note, however, that this total energy (it would be called the ''Bondi energy'' in general relativity), as well as its limit value, is always strictly larger than the energy of the original static monopole. This is because the expanding shells of oscillations store some part of the energy of the original pulse forever. In fact, this part of the energy cannot reach future null infinity since it is associated with the massive Yang-Mills field; moreover, as they are getting further and further away from the central region the monopole can get back less and less energy from them since nonlinear effects are getting to be more and more negligible. As it is shown in Sec. VII C 5, the energy stored by these expanding shells also approaches its nonzero asymptotic value from above following a power law time decay with exponent $-2/3$.

The time evolution of the frequency of oscillations of the excited monopole behaves also somewhat counter to general expectations. Consider first the fundamental frequency of the breathing monopole. Instead of having a slow decay in the frequency of the associated oscillations as their amplitude decreases there is an increase in the frequency which takes the maximum value at the ''end of time,'' i.e. at future timelike infinity. Interestingly, while the frequency of the breathing monopole tends to the mass of the Yang-Mills field from below the frequency of the oscillations stored in the expanding shell has no upper bound, although the amplitude is decreasing, as in case of the massive Klein-Gordon field [4]. Note that these phenomena are not at all unphysical. Recall that a simple physical system like the spinning coin on the desk can produce a quite similar effect. As energy loss happens due to dissipative processes, the amplitude of the ''spinning'' is getting smaller and smaller in consequence of which the frequency of the oscillations is getting higher and higher. In the case of the distant oscillating shells, the unbounded increase of the frequency is, in fact, to compensate the decrease of the oscillation amplitudes which together ensure the conservation of the energy stored by the shells.

By virtue of these results it seems not to be overrating to say that the investigation of the dynamics properties of magnetic monopoles made transparent a number of interesting and unexpected features of the underlying nonlinear system. Hopefully, these sorts of investigations will stimulate further numerical and analytic investigations of various similar nonlinear dynamical systems. For instance, partly motivated by the findings of the above described investigations, in a framework of linear perturbation theory some of the above mentioned features could be explained successfully both qualitatively and quantitatively [16]. Note, however, that truly nonlinear effects are by their very nature out of the scope of these sorts of investigations. In particular, as some of the new results of this paper make it transparent, they cannot be used to describe the behavior of the investigated system when the energy of the exciting pulse is much larger than that of the original static monopole.

Although in this paper we use our numerical code to describe various oscillations of a localized monopole, we would like to note that oscillations in a nonlinear theory may be responsible for the very existence of some compact objects. In a wide variety of nonlinear field theories, where no static soliton solutions exist, almost periodic long living oscillon configurations have been found. See for example [17–22] for recent results on this quickly evolving topic. A slightly modified version of our numerical code has also been used in [3] for a detailed study of oscillon configurations in ϕ^4 scalar theory.

The structure of this paper is as follows. In the next section, after recalling some of the basics related to the properties of the underlying generic dynamical system, a detailed description of the specific choice for both the YMH system and the geometry is provided. The static hyperboloidal conformal gauge applied in our investigations is introduced in Sec. III, while the first order representation of the field equations, relevant for the used conformal setting, is given in Sec. IV. A detailed description of the applied numerical scheme is presented in Sec. V, while various numerical tests of the code, for the case of massive and massless Klein-Gordon field, are presented in Sec. VI. Finally, all the numerical results concerning the evolution of dynamical magnetic monopoles, including subsections providing detailed descriptions of the time dependence of the basic and derived field variables and that of the frequency of the associated oscillations, the energy transfers, monitoring of the numerical violation of constraints and the energy conservation, along with the behavior of the radial and angular pressures, as well as the magnetic charge density, are presented in Sec. VII.

II. PRELIMINARIES

The investigated dynamical magnetic monopole is described as a coupled $SU(2)$ YMH system. The Yang-Mills field is represented by an $\mathfrak{su}(2)$-valued vector potential A_a and the associated 2-form field F_{ab} reads as

$$F_{ab} = \partial_a A_b - \partial_b A_a + ig[A_a, A_b], \tag{1}$$

where $[,]$ denotes the product in $\mathfrak{su}(2)$ and g stands for the gauge coupling constant. The Higgs field (in the adjoint representation) is given by an $\mathfrak{su}(2)$-valued function ψ while its gauge covariant derivative reads as $\mathcal{D}_a\psi = \partial_a\psi + ig[A_a, \psi]$. The dynamics of the investigated YMH system is determined by the action

$$S = \int \{\mathrm{Tr}(F_{ef}F^{ef}) + 2[\mathrm{Tr}(\mathcal{D}_e\psi\mathcal{D}^e\psi) - V(\psi)]\}\epsilon, \tag{2}$$

where ϵ is the four-dimensional volume element, moreover, $V(\psi)$, describing the self-interaction of the Higgs field, is chosen to be the standard quadratic potential

$$V(\psi) = \frac{\lambda}{4}[\mathrm{Tr}(\psi^2) - H_0^2]^2, \tag{3}$$

where λ and H_0 denote the Higgs self-coupling constant and the ''vacuum expectation value'' of the Higgs field, respectively.

The symmetric energy-momentum tensor of the considered YMH system takes the form

$$T_{ab} = -\frac{1}{4\pi}\left[\mathrm{Tr}(F_{ae}F_b^e) - \mathrm{Tr}(\mathcal{D}_a\psi\mathcal{D}_b\psi) + \frac{1}{4}g_{ab}\mathcal{L}\right], \tag{4}$$

where $\mathcal{L}$ stands for the Lagrangian

$$\mathcal{L} = \mathrm{Tr}(F_{ef}F^{ef}) + 2[\mathrm{Tr}(\mathcal{D}_e\psi\mathcal{D}^e\psi) - V(\psi)]. \tag{5}$$

A. Fixing the geometrical and gauge setup

This paper will investigate the evolution of spherically symmetric Yang-Mills–Higgs systems on a flat Minkowski background spacetime. Accordingly, as a fixed background, the four-dimensional Minkowski spacetime $(\mathbb{R}^4, \eta_{ab})$ will be applied, the line element of which in the conventionally used Descartes-type coordinates (x^0, x^1, x^2, x^3) reads as

$$ds^2 = (dx^0)^2 - (dx^1)^2 - (dx^2)^2 - (dx^3)^2. \tag{6}$$

The gauge group is specified by giving the set of generators $\{\tau_I\}$ $(I = 1, 2, 3)$ of the associated $\mathfrak{su}(2)$ Lie algebra which reads as

$$\tau_I = \tfrac{1}{2}\sigma_I, \tag{7}$$

where σ_I denote the Pauli matrices. The commutation relations relevant for this choice of generators are

$$[\tau_I, \tau_J] = i\varepsilon_{IJK}\tau_K, \tag{8}$$

where ε_{IJK} denotes the completely antisymmetric tensor with $\varepsilon_{123} = 1$.

In addition to the above special choice concerning the gauge group, our considerations will be restricted to YMH systems which are yielded by the ''minimal'' dynamical generalization of the static t' Hooft-Polyakov magnetic monopole configurations [14,23] (see also [24,25]). Accordingly, the Yang-Mills and Higgs field variables, $A_a = A_a^I\tau_I$ and $\psi = \psi^I\tau_I$, are specified in the Coulomb gauge via the relations

$$A_0^J = 0, \qquad A_I^J = \frac{(1-w)}{g}\varepsilon_{IJK}\frac{x^K}{r^2}, \tag{9}$$

$$\psi^I = H\frac{x^I}{r}, \tag{10}$$

where the functions w and H are assumed to be smooth functions in $\mathbb{R}^4$ depending upon the coordinates x^0, x^1, x^2, x^3 only in the combinations $t = x^0$ and $r = \sqrt{(x^1)^2 + (x^2)^2 + (x^3)^2}$. It is straightforward to check that both the Gauss and Lorentz gauge conditions are automatically satisfied by the above vector potential A_a.

Since the metric, as well as the matter fields, are required to be spherically symmetric, the use of the standard coordinates (t, r, θ, ϕ), adapted to the spherical symmetry of $(\mathbb{R}^4, \eta_{ab})$, is the most suitable. In these coordinates the line element of the Minkowski metric takes the form

$$ds^2 = dt^2 - dr^2 - r^2(d\theta^2 + \sin^2\theta d\phi^2). \tag{11}$$

We have assumed above that w and H are smooth functions of t and r. This might be surprising especially because our eventual aim is to carry out numerical simulations of the YMH systems under consideration. Numerical methods are inherently too rough to make a sensible distinction between configurations belonging to different differentiability classes. In fact, our smoothness assumption is to ensure certain technical conveniences used later and it is supported by the following considerations. (Note that for the following argument it would be enough to assume that w and H are smooth in a sufficiently small neighborhood of the origin.) In numerical simulation of spherically symmetric configurations a grid boundary representing the origin inevitably appears. This means that we need to solve an initial-boundary value problem which, in particular, requires the specification of "boundary behavior" of w and H at the origin throughout the time evolution. This is, in fact, the very point where we make use of our smoothness assumption. By virtue of (9) and (10) it is straightforward to see that spherical symmetry, along with the required smoothness of w and H through the origin, ensures that in a neighborhood of the origin w and H are even and odd functions of the r coordinate, respectively. Consequently, as it is described in Sec. V D in more detail, by extending our grid by a suitable number of virtual grid points the boundary values, for instance, of the r derivatives of w and H need not be specified by hand, instead they are naturally yielded by the time evolution of the corresponding odd and even functions.

The Yang-Mills field A_a as it is given by (9) is in the "Coulomb gauge." Another frequently used gauge representation is the so called "Abelian gauge" in which ψ has only one nonvanishing component, and which is achieved by making use of the gauge transformation

$$U = \exp(i\theta\tau_2)\exp(i\phi\tau_3). \tag{12}$$

A straightforward calculation yields that in the corresponding Abelian gauge the Yang-Mills and the Higgs fields read as

$$A_a = -\frac{1}{g}[w\{\tau_2(d\theta)_a - \tau_1\sin\theta(d\phi)_a\} + \tau_3\cos\theta(d\phi)_a] \tag{13}$$

and

$$\psi = H\tau_3. \tag{14}$$

The substitution of these gauge representations into the equations of motion, deducible from the action (2), yields the evolution equations for w and H which are given as

$$r^2\partial_t^2 w - r^2\partial_r^2 w = w[(w^2 - 1) + g^2 r^2 H^2], \tag{15}$$

$$r^2\partial_t^2 H + 2r\partial_r H - r^2\partial_r^2 H = H\left[2w^2 + \frac{\lambda}{2}r^2(H^2 - H_0^2)\right]. \tag{16}$$

The static finite energy solutions of these equations are called 't Hooft-Polyakov magnetic monopoles.

B. Regularity at the origin and at infinity

These equations, along with the former assumption concerning the smoothness of the basic variables, ensure certain regularity of the Yang-Mills and Higgs fields. In particular, it turned out that the values of w and H are restricted at the origin and at spacelike infinity throughout the evolution. At the origin (see Appendix A for more details) the relations

$$w(t, 0) = 1 \quad \text{and} \quad H(t, 0) = 0 \tag{17}$$

have to hold to have finite energy density, measured by the static observer with four velocity $u^a = (\partial/\partial t)^a$. In addition, whenever the smoothness of w and H is guaranteed in a neighborhood of the origin we also have

$$\partial_r^k w|_{r=0} = 0 \tag{18}$$

for k being odd, while

$$\partial_r^k H|_{r=0} = 0 \tag{19}$$

for k being even. At first sight it might be a bit of a surprise but a same type of reasoning that leads to (18) and (19) provides a restriction also for the rest of the derivatives. Namely, from the field equations and from the smoothness requirement it follows that at the origin all the nonvanishing derivatives $\partial_r^k w$, with $k \geq 4$, and $\partial_r^l H$, with $l \geq 3$, can be given as a function of $\partial_r^2 w$ and $\partial_r H$, along with their various time derivatives.

The argument associated with the regularity of the basic variables at spacelike infinity is more delicate. To get it we need to refer to the conformal (nonphysical) setting, where our numerical simulation actually will be carried out. In this framework it seems to be essential to assume that the fields are at least C^2 even through future null infinity, $\mathscr{I}^+$. We refer here to this requirement as being merely a technical assumption; nevertheless, we would like to emphasize that the use of it is supported by the following observations. In [26] it was proved that the time evolution of a massive Klein-Gordon field in Minkowski spacetime with initial data of compact support necessarily yields $\mathcal{O}(1/r^\infty)$ asymptotic behavior at null infinity. In addition, the results of Eardley and Moncrief [27–30] concerning the local and global existence of YMH fields in four-dimensional Minkowski spacetime supports that the above technical assumption can be deduced from the field equa-

tions at least in the case of suitably chosen initial data specifications.

This smoothness requirement, along with the relevant form of the rescaled field equations, implies (see Appendix A for more details) that w has to vanish while H has to be constant along the null geodesic generators of $\mathscr{I}^+$. The field equations also yield further restriction on this constant limit value H_∞ of H at $\mathscr{I}^+$. In particular, H_∞ must take the value H_0 whenever $\lambda \neq 0$ but it is an arbitrary (positive) constant, C, otherwise. Thus, by making use of a limiting argument, the values of w and H at spacelike infinity can be seen to be determined as

$$w_\infty = \lim_{r\to\infty} w(t, r) = 0, \tag{20}$$

$$H_\infty = \lim_{r\to\infty} H(t, r) = \begin{cases} H_0 & \text{if } \lambda \neq 0; \\ C & \text{otherwise.} \end{cases} \tag{21}$$

Notice that the later relations are in accordance with our general expectations that the considered dynamical YMH systems do really possess the asymptotic fall-off properties of a magnetic monopole [24,25] throughout the time evolution.

It follows from Eqs. (15), (16), and (21) that the semiclassical vector boson and Higgs mass, M_w and M_H, are

$$M_w = gH_\infty, \tag{22}$$

$$M_H = \sqrt{\lambda} H_\infty. \tag{23}$$

In particular, both fields are massless whenever H_∞ vanishes, while only the Higgs field is massless, although it is coupled to a massive vector boson, whenever the self-coupling constant λ is zero.

Whenever the smoothness of the basic variables is guaranteed through $\mathscr{I}^+$ then the nth order r derivatives of w and H are also restricted there. In particular, it follows from the relations (A10) and (A15)–(A18), along with the vanishing of the energy-momentum expressions at null infinity that whenever $H_\infty \neq 0$ the asymptotic fall-off conditions,

$$\lim_{r\to\infty} [r^{2n} \partial_r^n w(t, r)] = 0 \qquad (\text{for } n \geq 0) \tag{24}$$

and

$$\lim_{r\to\infty} [r^{2n} \partial_r^n H(t, r)] = 0, \qquad (\text{for } n \geq 2) \tag{25}$$

have to be satisfied.

It is important to note that whenever $\lambda = 0$, i.e. the self-coupling of the Higgs field is turned down, there exists an explicitly known [31] static solution to (15) and (16)

$$w_s = \frac{gCr}{\sinh(gCr)}, \tag{26}$$

$$H_s = C\left(\frac{1}{\tanh(gCr)} - \frac{1}{gCr}\right), \tag{27}$$

where C is an arbitrary positive constant which is in fact the limit value, H_∞, of the right-hand side of (27). This static solution is called the Bogomolny-Prasad-Sommerfield (BPS) magnetic monopole which is known to be a linearly stable configuration [32].

Notice that in the BPS limit, i.e. whenever $\lambda = 0$ and $H_\infty = H_0 \neq 0$, the Higgs field becomes massless and the only scale parameter of the system is the vector boson mass $M_w = gH_\infty$. Since in the case considered here $H_\infty \neq 0$, the rescalings $t \to \tilde{t} = tM_w$, $r \to \tilde{r} = rM_w$, and $H \to \tilde{H} = H/H_\infty$ transform the parameters to the value $g = H_\infty = 1$. This implies that whenever we would like to study the excitations of the BPS monopole it suffices to consider the time evolution of the system only for the particular choice of the parameters $g = H_\infty = 1$, because by inverse rescalings of these solutions all the possible solutions to the field equations can be generated. Actually, to check the efficiency of our numerical implementation of the evolution equations first the stability of this static solution was investigated. Later, the complete nonlinear evolution of systems yielded by strong impulse type excitations of these analytic static solutions was also studied in detail.

Although it is not necessary to be done, we preferred to put the principal part of (16) into the same form as the principal part of (15) which was achieved by making use of the substitution

$$H(t, r) = \frac{h(t, r)}{r} + H_\infty. \tag{28}$$

It follows then that our new basic variable h vanishes at the origin while it takes a finite limit value at infinity if H is guaranteed to tend to its boundary value fast enough there. The substitution of (28) into the relations (15) and (16) yields then

$$r^2(\partial_r^2 w - \partial_t^2 w) = w[(w^2 - 1) + g^2(h + H_\infty r)^2], \tag{29}$$

$$r^2(\partial_r^2 h - \partial_t^2 h) = (h + H_\infty r) \cdot \left[2w^2 + \frac{\lambda}{2}(h^2 + 2H_\infty rh)\right], \tag{30}$$

where we have used the relation $H_\infty = H_0$ whenever $\lambda \neq 0$. The regularity of the solutions to these equations at $r = 0$ follows from the boundary conditions (17). It is important to note that (21) and (28), along with our smoothness and symmetry assumptions, which, in particular, implies that H is an odd function of r, guarantees that $h + H_\infty r$ has to be an even function of the r coordinate. Moreover, since $h^2 + 2H_\infty rh = (h + H_\infty r)^2 - H_\infty^2 r^2$ the right-hand sides of (29) and (30) are both even functions of the r coordinate. Notice finally that, by Eqs. (29) and (30), the expressions $\partial_r^2 w - \partial_t^2 w$ and $\partial_r^2 h - \partial_t^2 h$ have regular limits at $r = \infty$ because, by virtue of (21), (24), (25), and (28), w and h remain finite while r tends to infinity.

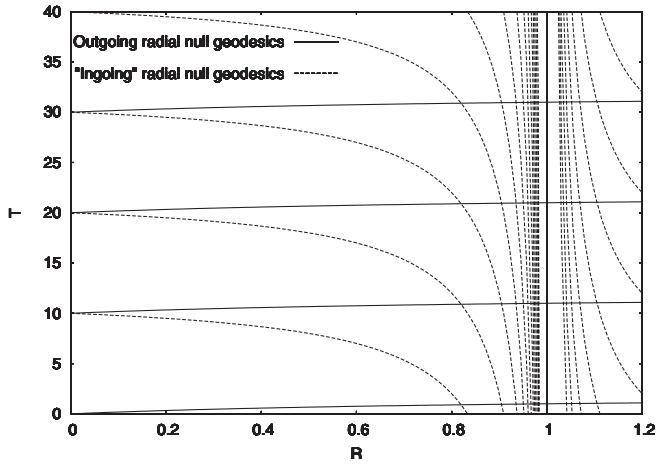

FIG. 1. The ingoing and outgoing radial null geodesic curves are shown in both the ''physical'' and ''unphysical'' regions. As in other conformal representations, each point represents a two-sphere of radius R. The interior of the strip $0 \leq R < 1$ corresponds to the original Minkowski spacetime while $\mathscr{I}^+$ is represented by the $R = 1$ coordinate line. Notice that the $R =$ const lines possesses a timelike character everywhere except at the $R = 1$ line which is null.

III. THE STATIC HYPERBOLOIDAL REFERENCE SYSTEM

In this section a conformal transformation of the Minkowski spacetime—along with the relevant form of the above matter field equations—will be considered.

The applied conformal transformation is a slightly modified version of the conformal transformation applied first by Moncrief [33] (see also [34,35]). It is defined by introducing the new coordinates (T, R) instead of (t, r) as

$$T(t, r) = \kappa t - \sqrt{\kappa^2 r^2 + 1}, \tag{31}$$

$$R(r) = \frac{\sqrt{\kappa^2 r^2 + 1} - 1}{\kappa r} \tag{32}$$

with the inverse relations

$$t = \frac{1}{\kappa}\left(T + \frac{1 + R^2}{1 - R^2}\right) \quad \text{and} \quad r = \frac{2R}{\kappa(1 - R^2)}, \tag{33}$$

where κ is an arbitrary positive constant. The Minkowski spacetime is covered by the coordinate domain satisfying the inequalities $-\infty < T < +\infty$ and $0 \leq R < 1$ (see Fig. 2).

The line element of the conformally rescaled metric $\tilde{g}_{ab} = \Omega^2 g_{ab}$ in coordinates (T, R, θ, ϕ) takes the form

$$d\tilde{s}^2 = \frac{\Omega^2}{\kappa^2} dT^2 + 2RdTdR - dR^2 - R^2(d\theta^2 + \sin^2\theta d\phi^2), \tag{34}$$

where the conformal factor is

$$\Omega(R) = \frac{\kappa}{2}(1 - R^2), \tag{35}$$

and, by (33) and (35), we have the relation

$$r\Omega = R. \tag{36}$$

In this conformal representation the $R = 1$ coordinate line represents $\mathscr{I}^+$ through which the metric $\tilde{g}_{ab}$ smoothly extends to the coordinate domain with $R \geq 1$.

The name ''static hyperboloidal gauge'' is explained by the following observations. First, (32) tells us that the $R =$ const lines represent world lines of ''static observers,'' i.e. integral curves of the vector field $(\partial/\partial t)^a$. Second, it follows from (31) that the $T =$ const hypersurfaces are, in fact, hyperboloids satisfying the relation $(\kappa t - T)^2 - \kappa^2 r^2 = 1$ in the Minkowski spacetime.

The equation describing radial null geodesics in the (T, R) coordinate system is independent of the parameter κ,

$$T = \frac{\pm 2R}{1 \pm R} + T_0, \tag{37}$$

with the plus signs corresponding to outgoing and the minus signs to ingoing geodesics. The form of the constant is chosen in a way that both type of geodesics cross the origin $R = 0$ at time $T = T_0$, see Fig. 1. The outgoing geodesic emanating from the origin reaches future null infinity $R = 1$ in a finite coordinate time at $T = T_0 + 1$. The ingoing geodesic starting from a point at radius R_0 at

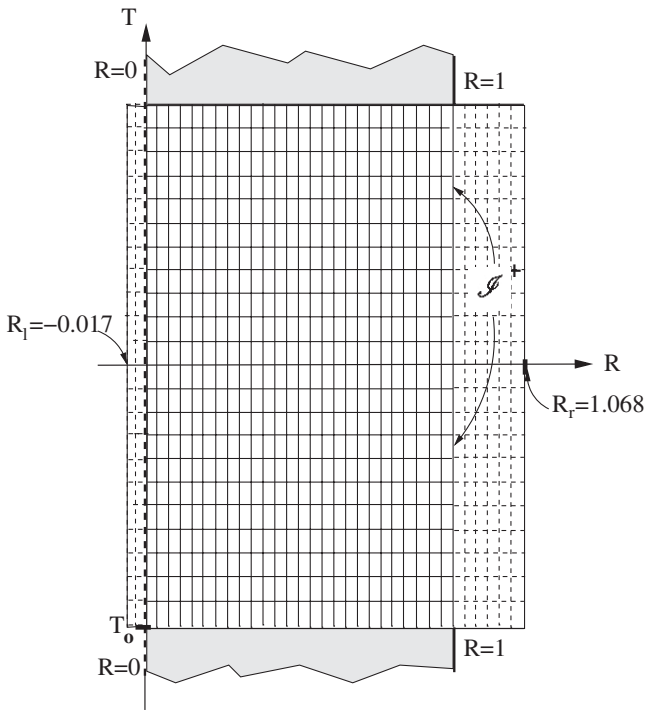

FIG. 2. The domains above the initial data hypersurface $T = T_0$ covered by the simplest possible orthogonal grid are indicated in the applied conformal representations.

$T = 0$ reaches the origin at $T = 2R_0/(1 - R_0)$. Consider now a geodesic starting at a point close to $\mathscr{I}^+$ with radius $R_0 = 1 - \delta R$. Such a geodesic reaches the origin at $T = -2 + 2/\delta R$. This means that for geodesics coming in from the far away region, the travel time essentially doubles when the geodesic starts from a point "twice as close" to the $R = 1$ line. This has an important consequence in relation to the validity domain of our numerical code. Namely, the doubling of the resolution yields the doubling of the time interval within which we may expect our numerical simulation to provide a proper solution to the selected problem. Here it is assumed tacitly that all the possible inaccuracies born at and coming from the outer region—that is the part of the spacetime where the evolution cannot be described properly by any of the numerical techniques based on a finite grid—travel inwards only with the speed of light.

Consider now the field equations relevant for this conformal setting. To start off take a function $f = f(t, r)$ of the coordinates t and r and denote by $\tilde{f} = \tilde{f}(T, R)$ the function $f(t(T, R), r(T, R))$ yielded by the substitution of (33) into f. A straightforward calculation justifies then that for any pair of functions $f = f(t, r)$ and $\tilde{f} = \tilde{f}(T, R)$ the relation

$$r^2(\partial_r^2 f - \partial_t^2 f) = \frac{4R^2}{(R^2+1)^2}\left(\frac{\Omega^2}{\kappa^2}\partial_R^2\tilde{f} - \partial_T^2\tilde{f} - 2R\partial_R\partial_T\tilde{f} - \frac{2\Omega}{\kappa(R^2+1)}\partial_T\tilde{f} - \frac{\Omega R(R^2+3)}{\kappa(R^2+1)}\partial_R\tilde{f}\right) \tag{38}$$

holds. It follows then from (36) and (38) that the field equations, (29) and (30), in the current conformal representation read as

$$\frac{4R^2}{(R^2+1)^2}\mathfrak{P}\tilde{w} = \tilde{w}[(\tilde{w}^2 - 1) + g^2(\tilde{h} + H_\infty R\Omega^{-1})^2], \tag{39}$$

$$\frac{4R^2}{(R^2+1)^2}\mathfrak{P}\tilde{h} = (\tilde{h} + H_\infty R\Omega^{-1}) \cdot \left[2\tilde{w}^2 + \frac{\lambda}{2}\tilde{h}(\tilde{h} + 2H_\infty R\Omega^{-1})\right], \tag{40}$$

where the second order partial differential operator $\mathfrak{P}$ is defined as

$$\mathfrak{P} = \frac{\Omega^2}{\kappa^2}\partial_R^2 - \partial_T^2 - 2R\partial_R\partial_T - \frac{2\Omega}{\kappa(R^2+1)}\partial_T - \frac{\Omega R(R^2+3)}{\kappa(R^2+1)}\partial_R. \tag{41}$$

As before, the regularity of the solutions to these equations at the origin, i.e. at $R = 0$ is guaranteed by the regularity of (29) and (30) at $r = 0$, while, the regularity at future null infinity, i.e. at $R = 1$, follows from (21), (24), and (25) provided that the fields have at least C^2 extensions through $\mathscr{I}^+$.

Hereafter, unless indicated otherwise, all the functions will be assumed to depend only on the coordinates T and R. Thereby we suppress all of the tildes, introduced above.

IV. THE FIRST ORDER HYPERBOLIC SYSTEMS

This section is to derive a first order hyperbolic system from the above evolution equations for which the initial value problem is well posed. To see that Eqs. (39) and (40) can be put into the form of a strongly hyperbolic system, we shall follow a standard process (see e.g. [36]). Correspondingly, first we introduce the first order derivatives of w and h,

$$w_T = \partial_T w, \qquad w_R = \partial_R w, \qquad h_T = \partial_T h, \qquad h_R = \partial_R h, \tag{42}$$

as new variables. In terms of the relevant enlarged set of dependent variables (39) and (40) can be given as

$$\partial_T w_T = \frac{\Omega^2}{\kappa^2}(\partial_R w_R) - 2R(\partial_R w_T) + b_w, \tag{43}$$

$$\partial_T h_T = \frac{\Omega^2}{\kappa^2}(\partial_R h_R) - 2R(\partial_R h_T) + b_h, \tag{44}$$

where b_w and b_h are given as

$$b_w = -\frac{2\Omega}{\kappa(R^2+1)}w_T - \frac{\Omega R(R^2+3)}{\kappa(R^2+1)}w_R - \frac{(R^2+1)^2}{4\Omega^2R^2}w[\Omega^2(w^2-1) + g^2(\Omega h + H_\infty R)^2], \tag{45}$$

$$b_h = -\frac{2\Omega}{\kappa(R^2+1)}h_T - \frac{\Omega R(R^2+3)}{\kappa(R^2+1)}h_R - \frac{(R^2+1)^2}{4\Omega^2R^2} \times (\Omega h + H_\infty R) \cdot \left[2\Omega w^2 + \frac{\lambda}{2}h(\Omega h + 2H_\infty R)\right]. \tag{46}$$

It is straightforward to see that the above equations, along with the first and third equations of (42), and the integrability conditions

$$\partial_T w_R = \partial_R w_T \quad \text{and} \quad \partial_T h_R = \partial_R h_T, \tag{47}$$

possess the form of a first order system

$$\partial_T \Phi = A_R(\partial_R \Phi) + B, \tag{48}$$

where Φ and B are given as

$$\Phi = \begin{pmatrix} w \\ w_T \\ w_R \\ h \\ h_T \\ h_R \end{pmatrix}, \qquad B = \begin{pmatrix} w_T \\ b_w \\ 0 \\ h_T \\ b_h \\ 0 \end{pmatrix}. \tag{49}$$

Moreover, A_R takes the form

$$A_R = \begin{pmatrix} 0 & 0 & 0 & 0 & 0 & 0 \\ 0 & -2R & \Omega^2/\kappa^2 & 0 & 0 & 0 \\ 0 & 1 & 0 & 0 & 0 & 0 \\ 0 & 0 & 0 & 0 & 0 & 0 \\ 0 & 0 & 0 & 0 & -2R & \Omega^2/\kappa^2 \\ 0 & 0 & 0 & 0 & 1 & 0 \end{pmatrix}. \tag{50}$$

Since the eigenvectors of A_R comprise a complete system and its eigenvalues are all real, this first order system is, in fact, a strongly hyperbolic system [11].

Notice also that B does not depend on the spacelike derivatives of Φ, i.e. it is a functional of T, R, and Φ exclusively, $B = B(T, R; \Phi)$. It is also straightforward to verify that the constraint equations, i.e. the second and the fourth equations of (42), are preserved by the time evolution governed by (48). This, in particular, guarantees that the pair of functions w and h yielded by the evolution of suitable initial data specifications will automatically satisfy the original evolution Eqs. (39) and (40) as well, provided that the constraint equations hold on the initial data surface.

Finally, we would like to emphasize that the system specified by the relations (48)–(50) is not only strongly hyperbolic but can be put into the form of a first order symmetric hyperbolic system. To see this, introduce the variables $\hat{w}_R$ and $\hat{h}_R$ by the relations

$$\hat{w}_R = \frac{\Omega}{\kappa} w_R \quad \text{and} \quad \hat{h}_R = \frac{\Omega}{\kappa} h_R. \tag{51}$$

Then the system of field equations for the vector variable $\Phi = (w, w_T, \hat{w}_R, h, h_T, \hat{h}_R)^T$ possess the form of (48) with

$$A_R = \begin{pmatrix} 0 & 0 & 0 & 0 & 0 & 0 \\ 0 & -2R & \Omega/\kappa & 0 & 0 & 0 \\ 0 & \Omega/\kappa & 0 & 0 & 0 & 0 \\ 0 & 0 & 0 & 0 & 0 & 0 \\ 0 & 0 & 0 & 0 & -2R & \Omega/\kappa \\ 0 & 0 & 0 & 0 & \Omega/\kappa & 0 \end{pmatrix}. \tag{52}$$

Nevertheless, in all of our numerical simulations, the strongly hyperbolic form given by (48)–(50) was used which system was found to be as efficient in accuracy in a number of particular cases as the symmetric hyperbolic system.

V. THE NUMERICAL SCHEME

In our numerical simulations we shall use the simplest possible orthogonal grid based on the $T = \text{const}$ and $R = \text{const}$ "lines" in the domain $T > T_0$ as it is indicated in Fig. 2. The relevant discrete set of grid points is given as

$$T_l = T_0 + l\Delta T, \qquad l = 0, 1, \ldots, L_{\max}, \tag{53}$$

$$R_i = i\Delta R, \qquad i = 0, 1, \ldots, I_{\max}, \tag{54}$$

for some $I_{\max}, L_{\max} \in \mathbb{N}$ fixed numbers and with the relation $\Delta T = k\Delta R$ for some $k \in \mathbb{N}$. In this setting a function $f = f(T, R)$ will be represented by its values at the indicated grid points, i.e. by $f^l_i = f(T_l, R_i)$.

In our numerical simulations, the total number of spatial grid points was chosen to be an integer power of 2, i.e. 2^N, for some value $N \in \mathbb{N}$. A small fragment of these spatial gridpoints were used to handle the grid boundaries at the origin and beyond future null infinity (see Sec. V D for more retails). For this purpose we always used $1/2^6$ and $1/2^4$ parts of the spatial gridpoints on the left side of the origin and beyond future null infinity. This means that the formal values of the R-coordinate at these timelike portions of the numerical grid boundaries are $R_l = -\frac{4}{256-4-16} \sim -0.017$ and $R_r = 1 + \frac{16}{256-4-16} \sim 1.068$. Note that the appropriate treatment of the grid boundaries does not require the use of fixed portions of the spatial gridpoints. Nevertheless, we used this simple approach to have a straightforward setting in which we could compare the results of our numerical simulations for various resolutions for the price that only the 236/256 part of the spatial gridpoints represented points from the original Minkowski spacetime.

A. The time integrator

The time integration of (48) is based on the use of the "method of lines" in a higher order scheme as it is proposed by Gustafsson *et al* [11]. In particular, we integrate (48), along the constant R_i lines, by making use of a fourth order Runge-Kutta scheme. This is done exactly in the manner as the Runge-Kutta scheme is used to integrate first order ordinary differential equations. Correspondingly, the value of Φ after a "time step" is determined as

$$\Phi^{l+1}_i = \Phi^l_i + \tfrac{1}{6}(\Psi^l_{(I)i} + 2\Psi^l_{(II)i} + 2\Psi^l_{(III)i} + \Psi^l_{(IV)i}), \tag{55}$$

where

$$\Psi^l_{(I)i} = \Delta T[A_R(\partial_R \Phi^l_i) + B(T_l, R_i; \Phi^l_i)], \tag{56}$$

$$\Psi^l_{(II)i} = \Delta T[A_R(\partial_R[\Phi^l_i + \tfrac{1}{2}\Psi^l_{(I)i}]) + B(T_l + \tfrac{1}{2}\Delta T, R_i; \Phi^l_i + \tfrac{1}{2}\Psi^l_{(I)i})], \tag{57}$$

$$\Psi^l_{(III)i} = \Delta T[A_R(\partial_R[\Phi^l_i + \tfrac{1}{2}\Psi^l_{(II)i}]) + B(T_l + \tfrac{1}{2}\Delta T, R_i; \Phi^l_i + \tfrac{1}{2}\Psi^l_{(II)i})], \quad (58)$$

$$\Psi^l_{(IV)i} = \Delta T[A_R(\partial_R[\Phi^l_i + \Psi^l_{(III)i}]) + B(T_l + \Delta T, R_i; \Phi^l_i + \Psi^l_{(III)i})]. \quad (59)$$

To be able to apply this method of time integration we must calculate R derivatives of certain functions several times. In this time integration process we approximated these R derivatives by a symmetric fourth order stencil (see Appendix B).

It follows from general considerations [11] that the above described time integration process applied to (48) cannot be stable unless a suitable dissipative term is added to each evaluation of the right-hand side of (48). An appropriate dissipative term, relevant for the fourth order Runge-Kutta scheme used here, reads as

$$\mathfrak{D} = \sigma(\Delta R)^5(\partial_R^6\Phi), \quad (60)$$

where σ is a nonnegative constant and the sixth order R derivatives were evaluated in a symmetric sixth order stencil (see Appendix B).

Notice that the use of this dissipative term does not reduce the order of accuracy of the applied finite difference approximation. Moreover, since (48) is an almost everywhere symmetrizable strongly hyperbolic system and all the differential operators are centered, it follows from Theorem 6.7.2. of [11] that the applied time integration process is stable provided σ is sufficiently large and $k = \Delta T/\Delta R$ is sufficiently small. Numerical experiments showed us that, for instance, the particular choices $\sigma \sim 10^{-2}$ and $k = 1/8$ provide the required stability for the time integration of our evolution equation.

B. The evaluation of the evolving fields at the origin and at future null infinity

Before being able to make the first time step, and later at each of the time levels, we have to face the following technical problem. The source term B in (48) contains terms—see the last terms of (45) and (46)—which are given as ratios of expressions vanishing at the origin and at conformal infinity, respectively. The evaluation of these types of expressions generally is a hard numerical problem.

It turned out, however, that the exact value of b_w and b_h is either irrelevant or can be shown to be zero. To see this consider first the evolution of the fields at the origin. By making use of the field equations and assuming that the fields are at least of class C^2 at $R = 0$ we have shown [see (17)–(19)] that in a sufficiently small neighborhood of $R = 0$ the field values w and h must possess the form

$$w = 1 + \hat{w}(T, R) \cdot R^2, \quad (61)$$

$$h = \hat{h}(T, R) \cdot R^2 - \frac{R}{\Omega}H_\infty, \quad (62)$$

where $\hat{w}(T, R)$ and $\hat{h}(T, R)$ are assumed to be sufficiently regular functions of their indicated variables. These relations immediately imply that

$$w(T, 0) \equiv 1, \quad (63)$$

$$w_T(T, 0) \equiv 0, \quad (64)$$

$$w_R(T, 0) \equiv 0, \quad (65)$$

moreover,

$$h(T, 0) \equiv 0, \quad (66)$$

$$h_T(T, 0) \equiv 0, \quad (67)$$

$$h_R(T, 0) \equiv -\frac{2H_\infty}{\kappa} \quad (68)$$

hold. In other words, the time evolution of our basic variables at the origin is trivial and hence the evaluation of the b_w and b_h is not needed there.

Despite their apparent singular behavior, the evaluation of b_w and b_h at $R = 1$ is possible based on the following observations. The first two terms of b_w and b_h are proportional to the conformal factor Ω so they vanish at $\mathscr{I}^+$. The last terms also vanish there in spite of the presence of the Ω^{-2} factors in them since these expressions always contain as a multiplying factor at least one of the massive field variables, either w or, whenever $\lambda \neq 0$, h. These field variables, however, possess the fall-off property that $r^n w$ and $r^n h$ for arbitrary positive integer value ($n \in \mathbb{N}$) tend to zero while $r \to \infty$. By making use of this fact, along with the relation $r = R/\Omega$, it is straightforward to check that both b_w and b_h must vanish at $\mathscr{I}^+$. Accordingly, the values of b_w and b_h were kept to be identically zero at $R = 1$ in the numerical simulations.

C. Increasing accuracy

In order to ensure higher order of accuracy we also have applied the following trick. Instead of calculating the time evolution of the variables w and h themselves, we determined the evolution of the deviation $w_\Delta = w - w_0$ and $h_\Delta = h - h_0$ of them with respect to certain analytic functions, w_0 and h_0. In fact, the functions w_0 and h_0 need not necessarily be required to be solutions of the field equations although it is favorable to assume that they possess the same type of behavior at $R = 0$ and at $\mathscr{I}^+$ as the functions w and h themselves. This way it was possible to achieve a considerable decrease of the error of our numerical scheme in these critical neighborhoods.

The evolution equations for w_Δ and h_Δ can be deduced immediately by making use of the assumptions that $w = w_\Delta + w_0$ and $h = h_\Delta + h_0$ satisfy (48). The linearity of

the involved differential operators yields that

$$\partial_T \Phi_\Delta = A_R(\partial_R \Phi_\Delta) + B_\Delta, \tag{69}$$

where

$$B_\Delta = B - \partial_T \Phi_0 + A_R(\partial_R \Phi_0) \tag{70}$$

with B being the functional as it is given by (49) but evaluated at the functions $w = w_\Delta + w_0$ and $h = h_\Delta + h_0$; moreover, Φ_Δ and Φ_0 denote the vectors

$$\Phi_\Delta = \begin{pmatrix} w_\Delta \\ (w_\Delta)_T \\ (w_\Delta)_R \\ h_\Delta \\ (h_\Delta)_T \\ (w_\Delta)_R \end{pmatrix}, \qquad \Phi_0 = \begin{pmatrix} w_0 \\ \partial_T w_0 \\ \partial_R w_0 \\ h_0 \\ \partial_T h_0 \\ \partial_R h_0 \end{pmatrix}. \tag{71}$$

It is straightforward to verify that in the particular case when w_0 and h_0 are solutions of (39) and (40), i.e. Φ_0 is a solution of (48),

$$B_\Delta = B - B_0 = \begin{pmatrix} (w_\Delta)_T \\ b_w - b_{w_0} \\ 0 \\ (h_\Delta)_T \\ b_h - b_{h_0} \\ 0 \end{pmatrix}, \tag{72}$$

where b_w and b_h are supposed to be evaluated at the functions $w = w_\Delta + w_0$ and $h = h_\Delta + h_0$, respectively. In all our numerical simulations presented in this paper, w_0 and h_0 were chosen to be the static BPS solution given by (26) and (27) with $C = g = 1$.

D. The treatment of the grid boundaries

In any numerical simulation the appropriate treatment of the grid boundaries requires the most careful considerations. In the case studied here the grid boundary consists of two disjoint parts, the gridpoints representing the origin and the right edge lying in the nonphysical spacetime region. It is the evaluation of various derivatives of the dependent variables at these boundaries that demand very careful investigations. The handling of these issues, as they are implemented in our code, are described in the following subsections.

1. The boundary at the origin

As it was already mentioned in Sec. II A, at the origin we can use spherical symmetry and the smoothness of the field variables to gain information about the parity of the relevant functions. This knowledge can then be used to extend these functions onto a *virtually* enlarged grid. In particular, for any function which can be divided into two parts, one of which has a definite parity in coordinate R, while the other part is explicitly known, suitable symmetry transformations can be used to define values of the function at the additional grid points to the left of the word line representing the origin (see Fig. 3). By making use of these values the required number of R derivatives of the applied variables can be determined at $R = 0$. More explicitly, as we will see, any function f in our interest can be given as a sum of two functions, $f = f^{d.p.} + f^{e.k.}$, one of which has a definite parity $f^{d.p.}$, being either even or odd function of the R coordinate, and another explicitly known one $f^{e.k.}$. Such a function can be extended, its extension will be denoted by $\{f\}^{\text{ext}}$, to the additional grid points as follows. Suppose, first, that $f^{d.p.}$ is an even function. Then $f^{\text{even}} = f - f^{e.k.}$ can be extended to the left of $R = 0$ simply by taking the axial reflection, $\{f^{\text{even}}\}^{\text{ext}} = (f - f^{e.k.})^{AR}$, of its graph to the $R = 0$ axis, defined by the relation $(f^{\text{even}})^{AR}|_{-i} = f_i^{\text{even}}$. Finally, by making use of the fact that $f^{e.k.}$ is explicitly known and thereby its extension is supposed to be also known (potential singularities at the origin have already been excluded by former assumptions), the extension $\{f\}^{\text{ext}}$ of f can be given as $\{f\}^{\text{ext}} = (f - f^{e.k.})^{AR} + \{f^{e.k.}\}^{\text{ext}}$. A similar process applies whenever $f^{d.p.}$ is an odd function with the distinction that axial reflection should be replaced by a "central reflection" determined by the relation $(f^{\text{odd}})^{CR}|_{-i} = -f_i^{\text{odd}}$. Thereby the extension of f then can be given as $\{f\}^{\text{ext}} = (f - f^{e.k.})^{CR} + \{f^{e.k.}\}^{\text{ext}}$.

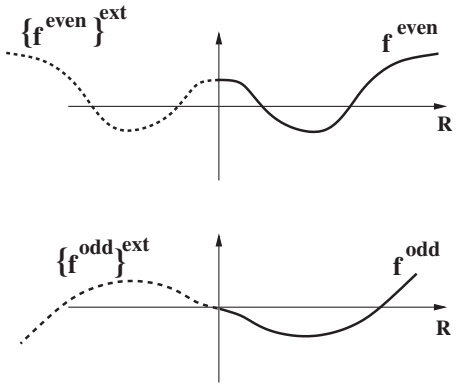

FIG. 3. The way of extension of functions to $R < 0$ is indicated for even, f^{even}, and odd, f^{odd}, functions, respectively. In fact, the extensions are determined by either an axial or a central reflection to the $R = 0$ line or to the "central point" as indicated by the formulas $\{f^{\text{even}}\}^{\text{ext}}|_{-i} = f_i^{\text{even}}$ and $\{f^{\text{odd}}\}^{\text{ext}}|_{-i} = -f_i^{\text{odd}}$, respectively.

Turning back to our concrete field variables, note first that in the time integration process we need to evaluate R derivatives of the dependent variables listed as components of the vector valued functions Φ; see the relation (49). Since w and $h + rH_\infty$ were found to be even functions of the original r coordinate, it follows by a straightforward substitution that

$$w = w^{\text{even}}, \tag{73}$$

$$w_T = w_T^{\text{even}}, \tag{74}$$

$$w_R = w_R^{\text{odd}}, \tag{75}$$

$$h = h^{\text{even}} - \frac{R}{\Omega} H_\infty, \tag{76}$$

$$h_T = h_T^{\text{even}}, \tag{77}$$

$$h_R = h_R^{\text{odd}} - \frac{1+R^2}{2\Omega^2} H_\infty. \tag{78}$$

Thereby the extensions of these functions, to the enlarged grid, yielded by the above described general process are

$$w^l_{-i} = w^l_i, \tag{79}$$

$$w^l_{T-i} = w^l_{Ti}, \tag{80}$$

$$w^l_{R-i} = -w^l_{Ri}, \tag{81}$$

$$h^l_{-i} = h^l_i + 2H_\infty \left(\frac{R}{\Omega}\right)^l_i, \tag{82}$$

$$h^l_{T-i} = h^l_{Ti}, \tag{83}$$

$$h^l_{R-i} = -h^l_{Ri} - H_\infty \left(\frac{1+R^2}{\Omega^2}\right)^l_i. \tag{84}$$

Note that whenever we consider the evolution of $\Delta\Phi$ with respect to a solution Φ_0 of (48)—Φ_0 possesses the same parity properties as the hypothetical solution Φ itself—the components of $\Delta\Phi$ are necessarily even functions of the R coordinate so their extensions at the origin are straightforward.

2. The grid boundary in the nonphysical spacetime

The appropriate treatment of the boundary in the nonphysical spacetime requires completely different types of considerations. Clearly, at this part of the boundary there is no way to enlarge the grid based on a suitable combination of certain smoothness and symmetry requirements, as it was possible to be done at the origin. Instead, to be able to determine the required number of R derivatives we used the following two ideas:

First, at the edge and neighboring grid points we applied a numerical adaptation called "one-sided derivatives" (see Appendix B) in analytic investigations. By making use of these approximations the time integration process can be carried out along the grid lines close to the edge. Second, our problem inherently is a boundary initial value problem (see e.g. [11]). Thus appropriate boundary conditions have to be chosen at the grid boundary to be able to carry on the time integration scheme. There is a considerable freedom in choosing boundary conditions at the edge of the grid. We intended to choose the one which allows waves to travel from the left toward the edge of the grid without being reflected, moreover, which excludes waves coming from beyond this edge toward the direction of the domain of computation. The corresponding restrictions in terms of our basic variables in the static hyperboloidal gauge are

$$w_T = -\tfrac{1}{2}(R+1)^2 w_R, \tag{85}$$

$$h_T = -\tfrac{1}{2}(R+1)^2 h_R. \tag{86}$$

The above described treatment seems to be too simple-minded and one may doubt whether it is useful in the presence of the massive nonlinear YM field, w, which could, in principle, produce arbitrary frequency of oscillating modes. In this respect it is worth keeping in mind the following. Consider the part of the initial data surface T_0 beyond $\mathscr{I}^+$ combined with the part of $\mathscr{I}^+$ to the future of T_0. The resulted hypersurface may be used as an initial data surface to study the evolution beyond $\mathscr{I}^+$. Since the massive field w decays exponentially towards $\mathscr{I}^+$, moreover, w was chosen to be zero on T_0 beyond $\mathscr{I}^+$, we have that the initial data for w on the above specified initial data surface is identically zero. This, however, by virtue of (39) implies that in the analytic case w has to be identically zero at least in a sufficiently small neighborhood of $\mathscr{I}^+$ on the nonphysical side of $\mathscr{I}^+$. Notice also that the above imposed conditions do fit to the massless Higgs field as well. We would like to emphasize that this simple analytic reasoning had also been justified by our numerical simulations where the absolute value $|w|$ of w remained always smaller than 10^{-28} for the entire evolution beyond $\mathscr{I}^+$.

E. Specific choices of parameters in the code

In order to concentrate a sufficient number of grid points to the central region where the monopole lives, as well as to have enough grid points to resolve the expanding shell structures at large radius, we have chosen $\kappa = 0.05$ as the parameter included in the coordinate transformation (31) and (32). This specific choice turned out to be appropriate for all the simulations presented in this paper.

For convenience, the total number of spatial grid points was always chosen to be an integer power of 2. Our minimal resolution was $2^8 = 256$, with 4 points in the negative R region and 16 points in the $R > 1$ domain. To preserve the grid point positions when doubling the resolution, in general, we used $4/256 = 1/64$ part of the total spatial grid points for the negative R mirror image points, and $16/256 = 1/16$ part of the total points for the unphysical domain. Keeping the "size" of the unphysical region above $R > 1$ to be constant is useful when investigating the stability and the convergence of the code in that region, while the unnecessary points in the negative R domain only decrease the speed of the code slightly.

In order to investigate the stability conditions of the numerical code, it is helpful to write out the coordinate velocity of the radial null geodesics. Using (37) we get

$$\frac{dR}{dT} = \pm\frac{1}{2}(1 \pm R)^2, \tag{87}$$

where the positive signs correspond to outgoing and the negative signs to ingoing geodesics. The maximal coordinate velocity occurs at null infinity $R = 1$, taking the value 2 for outgoing geodesics. The absolute value of the coordinate velocity of ingoing geodesics is always smaller than $1/2$. In principle this would allow any numerical time step ΔT which is smaller than half of the radial step ΔR. However, the evolution equations of the massive field components have an apparent singularity at $R = 1$, where our numerical evolution code was not appropriately stable unless the time step was chosen as small as $\Delta T = \Delta R/8$.

Choosing the parameter σ in the dissipative term (60) to be $\sigma = 0.01$ stabilized our numerical code without influencing the results significantly, even at lower resolutions.

VI. TESTING THE NUMERICAL CODE WITH MASSIVE AND MASSLESS KLEIN-GORDON FIELDS

In order to ascertain the appropriateness of our numerical code we employed it to a physical system for which the time evolution can be established by an independent, certainly more precise method. Because of the linearity of the equations describing the massive Klein-Gordon field, its time evolution can be calculated by the Green function method. If the Klein-Gordon field and its derivative are given on a spacelike hypersurface then the field value can be calculated at any point in the future as a sum of two definite (numerical) integrals (for more details see, e.g., [4]). The study of the Klein-Gordon field is especially important, since for several physically important systems, including the magnetic monopole, at large radius the various field components decouple, and behave like independent massive or massless linear Klein-Gordon fields.

In the spherically symmetric case the Klein-Gordon field Φ satisfies the wave equation

$$\partial_r^2\Phi + \frac{2}{r}\partial_r\Phi - \partial_t^2\Phi = m^2\Phi. \tag{88}$$

Introducing the new field variable $z = r\Phi$, in the coordinate system (T, R) defined by (31) and (32) the Klein-Gordon equation takes the form

$$\mathfrak{P}\, z = \frac{(R^2+1)^2}{4\Omega^2}m^2 z, \tag{89}$$

where the differential operator $\mathfrak{P}$ is defined in (41). Similarly to the monopole case the equation can be transformed to a system of three first order partial differential equations by introducing the new dependent variables $z_T = \partial_T z$ and $z_R = \partial_R z$.

The initial data on the $T = 0$ hypersurface was chosen as a specification of a nonzero time derivative in a localized region superimposed on the vacuum value of the field $z = 0$ as

$$(z_T)_\circ = \begin{cases} \frac{c}{\kappa}\exp[\frac{d}{(r-a)^2-b^2}], & \text{if } r \in [a-b, a+b]; \\ 0, & \text{otherwise,} \end{cases} \tag{90}$$

with the constants selected to be $a = 2$, $b = 1.5$, $c = 70$, $d = 10$, and $\kappa = 0.05$ in this section.

First, we applied our evolution code to the massive Klein-Gordon field with $m = 1$. On Fig. 4 we compare the field values on a constant T slice obtained with different spatial resolutions to the precise value calculated by the Green function method. The chosen time slice is at $T = 2.4746$, well after the null geodesic emanating from the origin at $T = 0$ has reached null infinity at $T = 1$. It is apparent that even if the results obtained by the evolution code are not completely satisfactory close to $\mathscr{I}^+$ $(R = 1)$ the field values in the central area remain correct for considerably longer time intervals. In Fig. 5 the upper envelope curve for Φ is shown at a fixed radius, $R = 0.025\,42$, corresponding to $r = 1.0176$. The frequency of the field oscillations approaches (from above) $m = 1$ in terms of the original time coordinate t, which in the T

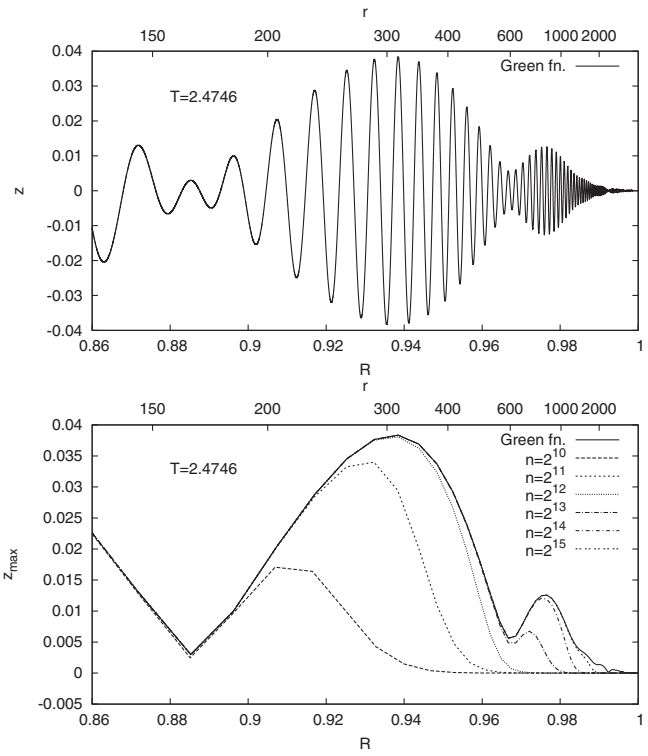

FIG. 4. The behavior of the massive Klein-Gordon field with $m = 1$ at the $T = 2.4746$ slice for large radii. In order to make the expanding shell structures more apparent, the function $z = r\Phi$ is plotted instead of Φ. Upper graph: the oscillations of z as calculated by the Green function method. Lower graph: the upper envelope of the oscillations in z, i.e. the curve connecting the maximum points of the function z, for the Green function calculation, and also for the evolution code corresponding to the indicated spatial resolutions.

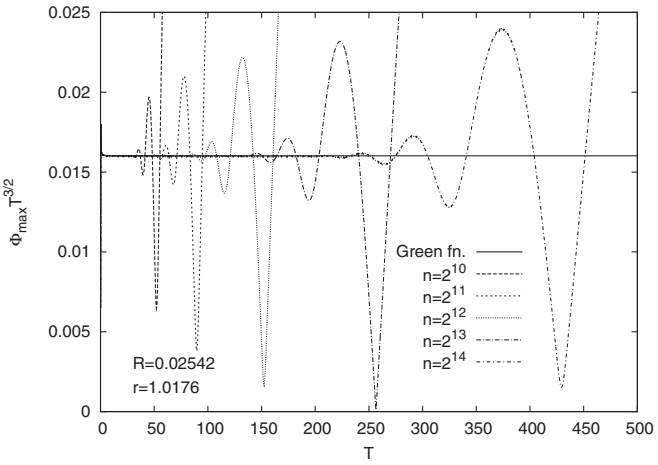

FIG. 5. The upper envelope curve of the oscillations of the Klein-Gordon field Φ at a constant radius close to the center of symmetry. In order to compensate for the fast decay of the field, the envelope of $\Phi T^{3/2}$ is plotted, which should tend to a constant value on theoretical grounds. Apart from a short initial period, the envelope of the Green function result is really constant. The envelopes of the functions obtained by the evolution code stay near this constant value for longer and longer times as the number of spatial grid points increases.

coordinate corresponds to 20. We can see that as it may be expected from the behavior of the ingoing null geodesics, the doubling of the resolution increases the time interval

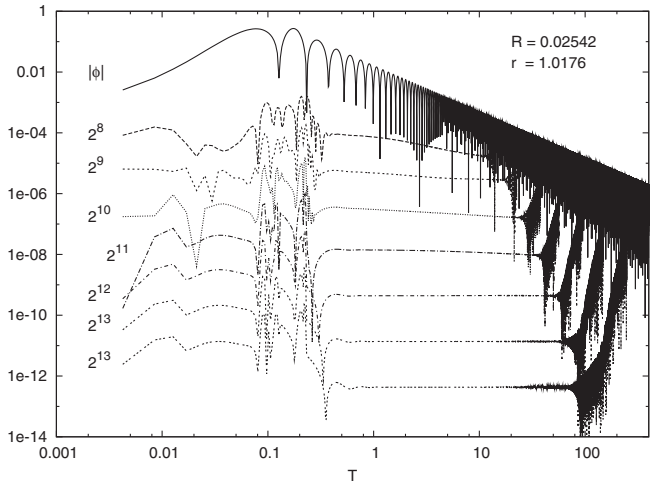

FIG. 6. Logarithmic plot of the absolute error of the value of the massive Klein-Gordon field ϕ at constant radius $R = 0.025\,42$ calculated with several different numerical resolutions corresponding to the indicated number of spatial grid points. The correct absolute value of the field is also plotted in order to show the time intervals where the error is smaller than the actual function value. We note that the downward pointing peaks indicate moments of time where the functions change signature. In order to reduce the complexity of the figure, for each resolution the error is plotted only up to a time where it becomes close to the exact value.

where the numerical solution is valid approximately by a factor of 2. In Fig. 6 the absolute value of the error at the same constant R radius is shown for several different numerical resolutions. Initially, up to approximately $T = 0.1$, the error values decrease according to the expected fourth order convergence of the code. Later, for $T > 0.3$ the convergence became even faster, approximately fifth order. This behavior is due to dominance of the artificial dissipation term which decreases as $(\Delta R)^5$. At later stages a numerical instability arises and the error increases until its absolute value reaches the magnitude of ϕ and the numerical simulation is no longer reliable.

We have also tested our code by applying it to the massless Klein-Gordon field with the same parameters in the initial data (90). With $m = 0$ the Klein-Gordon Eq. (89) is regular at null infinity $R = 1$ in the compactified representation. In Fig. 7 we show the rescaled field variable $z = r\Phi$ at null infinity as a function of the hyperboloidal time coordinate T obtained with several different numerical resolutions. Since in the massless case information spreads strictly with the velocity of light, the value of z has to be exactly zero before the outgoing light ray from the outer edge of the nonzero initial data, i.e. from $T = 0$ and $r_b = a + b$, reaches null infinity, and has to return to zero again after the ingoing ray from the same point, bouncing through the center, reaches null infinity as well. This means that the signal can be nonzero only within the time interval $\sqrt{\kappa^2 r_b^2 + 1} - \kappa r_b < T < \sqrt{\kappa^2 r_b^2 + 1} + \kappa r_b$ which, after substituting the values of the constants κ and r_b, corresponds to the interval $0.8402 < T < 1.1902$. We see that the higher the resolution is the better the numerical simulation can follow the abrupt changes in the magnitude of the field variable. Another feature that can be seen from the figure is that after the signal left the system a numerical

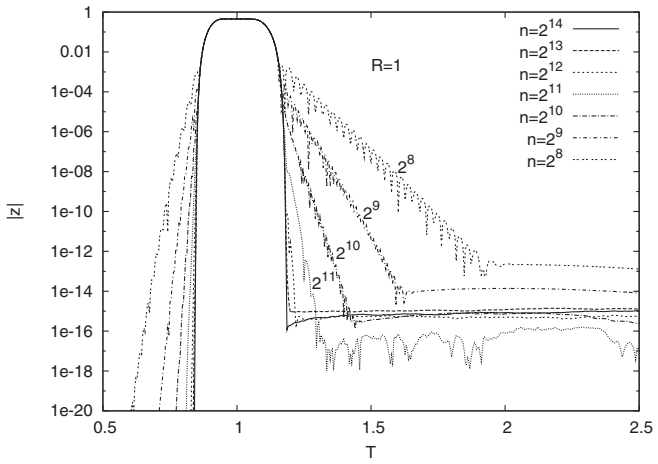

FIG. 7. Time dependence of the absolute value of the rescaled field variable $z = r\Phi$ at null infinity $R = 1$ obtained by our numerical code in case of the massless Klein-Gordon field with numerical resolutions corresponding to the indicated number of spatial grid points.

noise remains, with a magnitude of about 10^{-16} part of the size of the initial data. The size of this noise remains in this low range for very long time intervals, even for $T \approx 10^4$.

In order to keep the numerical noise at a low level for very long time intervals, a smooth cutoff in the artificial dissipation term has been introduced in the unphysical region $R > 1$. This was necessary because of the incompatibility of the sixth derivative dissipative term with the outgoing boundary condition applied at the outer edge of the grid.

VII. NUMERICAL RESULTS FOR THE TIME EVOLUTION OF MAGNETIC MONOPOLES

A. Choice of initial data

The numerical simulations presented in this paper were carried out in the $\lambda = 0$ case, when the Higgs field is massless and the static monopole solution is given by w_s and H_s in (26) and (27). For our numerical simulations we used initial data which consisted of a concentrated spherically symmetric pulse superposed on the static monopole solution. Defining $h_s = r(H_s - H_\infty)$, at $T = 0$ we choose $(w)_\circ = w_s$, $(w_R)_\circ = \partial_R w_s$, $(h)_\circ = h_s$, $(h_R)_\circ = \partial_R h_s$, $(h_T)_\circ = 0$, and

$$(w_T)_\circ = \begin{cases} \frac{c}{\kappa} \exp[\frac{d}{(r-a)^2 - b^2}], & \text{if } r \in [a-b, a+b]; \\ 0, & \text{otherwise.} \end{cases} \tag{91}$$

In all of the following simulations we take $a = 2$, $b = 1.5$, and $d = 10$, but we choose different amplitudes c. As is indicated by Table I, for instance, for our basic choice $c = 70$, which is the case discussed in [5], the energy provided by the pulse is about 55% of the energy of the background static monopole solution. Notice, however, that for $c = 280$ the energy of the pulse gets to be 16 times the energy of $E_{c=70}$ which implies that the energy of the pulse is 887% of the energy of the original static BPS monopole. Clearly such an excitation is far too strong to be considered as a perturbation and, as we shall see below, highly nonlinear aspects of the evolution show up in this case.

TABLE I. The energy E_c of the initial pulse, its ratio to the static monopole energy, i.e. E_c/E_s, and the fraction of the energy radiated to $\mathscr{I}^+$ up to time $T = 300$ and $T = \infty$ are given for five different values of the initial amplitude parameter c. The energy of the original static BPS solution is $E_s = 12.566\,37$.

c	E_c	E_c/E_s	S_{300}/E_c	S_∞/E_c
0.7	0.000 696 595	0.000 055 43	0.477 93	0.480 14
7	0.069 659 5	0.005 543	0.474 28	0.476 46
70	6.965 95	0.5543	0.440 37	0.442 50
280	111.455	8.869	0.563 88	0.5725
1120	1783.28	141.9	0.851 77	0.8555

B. The qualitative picture

Before presenting an accurate and comprehensive quantitative analysis of the dynamics of the excited monopole, it is informative to consider the qualitative aspects of the investigated processes. This is done in this section by making use of *spacetime plots* of various quantities, where the term "spacetime plot" is to indicate that the quantity in question is given as a function of space and time always over a rectangular coordinate domain of the (R, T) plane. Accordingly, on these spacetime plots the horizontal lines will always represent the $T =$ const coordinate lines, along which the value of the R coordinate is changing between the indicated minimal and maximal values, $R_{\min} \le R \le R_{\max}$, increasing from the left to right. Similarly, the vertical lines are the $R =$ const coordinate lines, along which the value of the T coordinate is changing between the indicated initial and final values, $T_i \le T \le T_f$, increasing from the bottom to the top.

1. The evolution of the basic variables

This short subsection is to present some spacetime plots informing the reader about the behavior of the basic variables w and h as the monopole reacts for weak and strong excitations.

There are immediate similarities and differences to be observed. First, the basic features indicated by Figs. 8–11 are similar although the energy of the exciting pulse relative to the energy of the initially static BPS monopole is negligible for the weak excitation—that is why not the field values w and h themselves but their difference with respect to the static background are plotted on Figs. 8 and 9—while it is about 9 times of the energy of the BPS

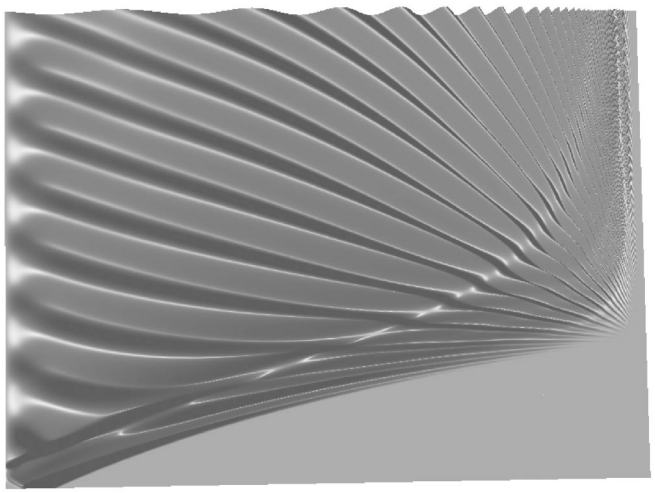

FIG. 8. The spacetime plot of the difference $w - w_0$ between the dynamical and the static values of the field variable w for the weak excitation with $c = 0.7$ while T and R take values from the intervals $0 < T < 2.9661$ and $0 \le R \le 1$. The maximum, the minimum, and the average values of $w - w_0$ are 0.004 230, $-0.002\,398$, and $9.021 \cdot 10^{-6}$.

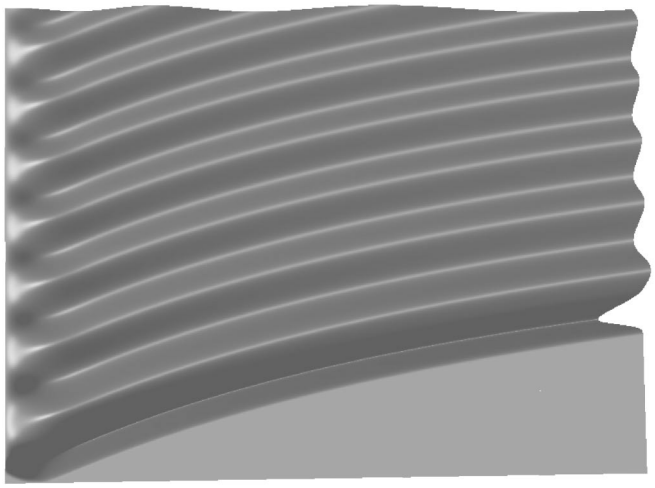

FIG. 9. The spacetime plot of the difference $h - h_0$ between the dynamical and the static values of the field variable h for the weak excitation with $c = 0.7$ while T and R take values from the intervals $0 \leq T \leq 2.9661$ and $0 \leq R \leq 1$. The maximum, the minimum, and the average values of $h - h_0$ are 0.000 963 2, $-0.004\,673$, and $-0.000\,173\,8$.

monopole for the strong excitation. In spite of the immediate similarities, the frequencies of the developing oscillations at the center are different. It is a bit of surprise that the larger the excitation is the lower the initial frequency. Comparing the w and h evolutions, the most important differences get manifested if one considers the shape of the curved lines associated with the maximum and minimum field values. While these curves seem to approximate ingoing null geodesics in case of the massive Yang-Mills field, see Figs. 8 and 10, they closely follow outgoing null rays in case of the massless Higgs field as indicated by Figs. 9 and 11. Since all physically interesting quantities

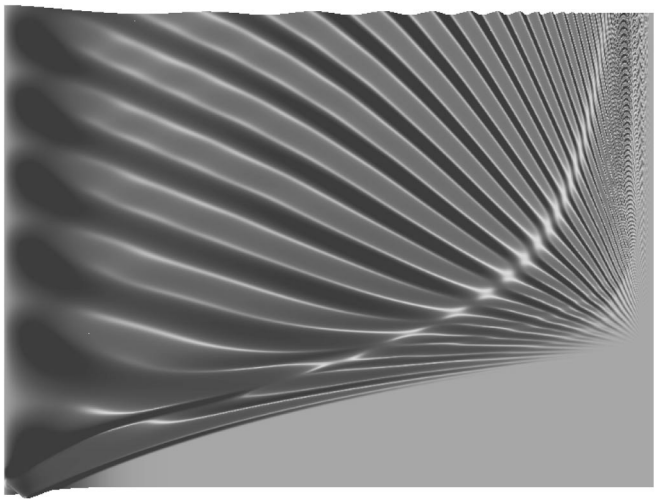

FIG. 10. The spacetime plot of w for the strong excitation with $c = 280$ while T and R take values from the intervals $0 \leq T \leq 2.9661$ and $0 \leq R \leq 1$. The maximum, the minimum, and the average values of w are 2.070, -1.210, and 0.073 46.

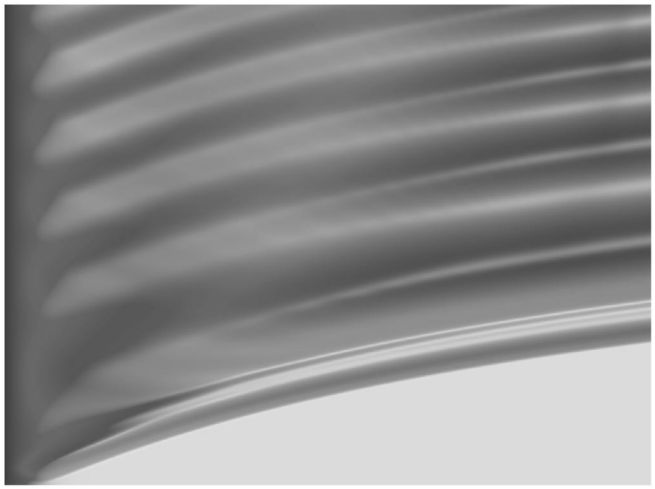

FIG. 11. The spacetime plot of h for the strong excitation with $c = 280$ while T and R take values from the intervals $0 \leq T \leq 2.9661$ and $0 \leq R \leq 1$. The maximum, the minimum, and the average values of h are -5.317, 0, and -3.034.

like the energy, energy current, or magnetic charge densities are derived from w and h, along with their derivatives, these derived quantities shall show a mixture of these clear characters as it will be seen below.

These figures make it also transparent that the two basic variables w and h, although strongly coupled in the central region, can be considered as being independent far away from there.

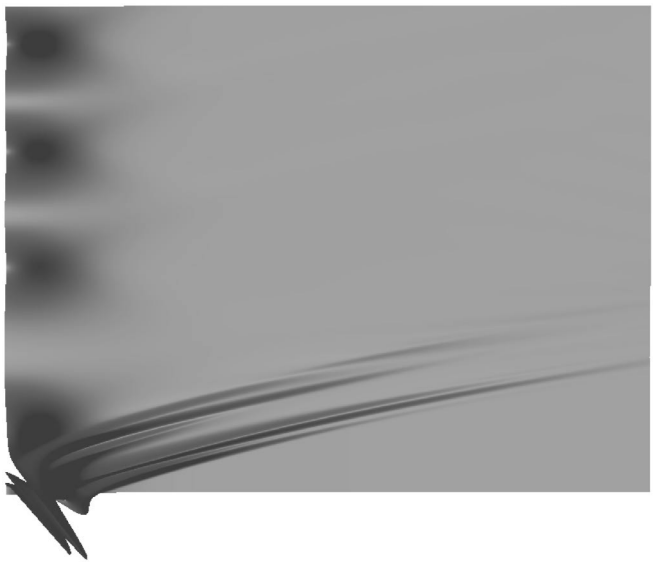

FIG. 12. The spacetime plot of the energy density $\varepsilon = T_{ab}t^a t^b$ for a strong excitation with amplitude $c = 280$ and for the space and time intervals $0 \leq R \leq 0.4915$ and $0 \leq T \leq 2.119$. The maximum, the minimum, and the average values of ε are 13.33, $2.214 \cdot 10^{-6}$, and 0.038 45.

2. The spacetime dependence of energy and energy transfer

One might expect that the most natural quantity to be applied when one tries to present the evolution of a system is the spacetime plot of the energy density. Such a quantity has a meaning only after the family of observers measuring it has been specified. In our setting it is natural to consider the energy density measured by static observers represented by the unit timelike Killing vector field $t^a = (\partial/\partial t)^a$. Let us denote by ε the associated energy density which can be given by the relation $\varepsilon = T_{ab}t^a t^b$.

Figure 12 is included to make it clear that even for a large excitation the information concerning the dynamics of the system is not properly reflected by the energy density. There is a clearly visible huge pulse at the beginning, the top of the peak is pointing far out from the plane of the figure at the lower left corner, which is followed by a moderated oscillation at the very center. Although the range of the radial coordinate is now only $0 \le R \le 0.4915$, corresponding to $0 \le r \le 25.92$, it is easy to agree that beside the short dynamical starting the details of the evolution are less transparent on most of this figure.

Upon investigating the system, it turned out that instead of monitoring the behavior of the energy density ε it is more informative to consider the time evolution of the energy density $\mathcal{E} = \mathcal{E}(T, R)$ "associated with shells of radius R," defined by

$$\mathcal{E} = 4\pi r^2 \frac{dr}{dR} T^0_0 = 2\pi\kappa(R^2+1)\frac{R^2}{\Omega^4} T^0_0, \qquad (92)$$

where the components of the energy-momentum tensor (4) are calculated in the coordinate system $x^a = (T, R, \theta, \phi)$. Justification of this definition will be given in Sec. VII C 2, where the energy conservation will be considered in detail. The integral, $\int_0^1 \mathcal{E} dR$, with respect to the R coordinate gives, for any fixed value of T, the total energy $E(T)$ of the $T =$ const hypersurface.

The advantages related to the use of $\mathcal{E}$, instead of ε, are visible on Fig. 13. This spacetime plot of $\mathcal{E}$ is already very informative; it clearly manifests the most important characteristic features of the beginning of the evolution. First there is a direct energy transport to $\mathscr{I}^+$ (represented by the right vertical edge) by the massless Higgs field following outgoing null geodesics. The second phenomenon is that right after a short period a quasistable oscillation starts at the central region (close to the left vertical edge). Finally, the formation of the expanding shells of high frequency oscillations in the distant region is also clearly visible. The time dependence of the mean value, the amplitude, and frequency of some of the oscillating quantities will be investigated in detail in Sec. VII C 6.

To understand the evolution of the investigated system it is also important to consider spacetime plots giving information about the energy transfers represented by the energy current density associated with shells of radius R,

$$\mathcal{S} = 4\pi r^2 \frac{dr}{dR} T^1_0 = 2\pi\kappa(R^2+1)\frac{R^2}{\Omega^4} T^1_0. \qquad (93)$$

Referring to the results contained by Sec. VII C 2, it can also be justified that $\mathcal{S}$ is the quantity, the time integral $\int_{T_2}^{T_1} \mathcal{S} dT$ of which, for any fixed value of R, gives the energy passing though the $R =$ const hypersurface during the time interval $T_1 \le T \le T_2$.

Figure 14 shows the spacetime plot of $\mathcal{S}$ for the case of the intermediate energy exciting pulse with $c = 70$. The

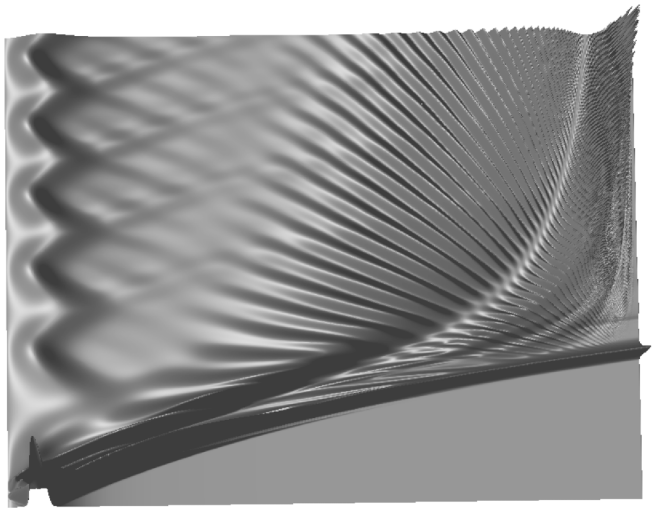

FIG. 13. The spacetime plot of $\mathcal{E}$ for the large excitation with $c = 280$ for the space and time intervals $0 \le R \le 1$ and $0 \le T \le 2.9661$. The maximum, the minimum, and the average values of $\mathcal{E}$ are 5572, 0, and 96.68.

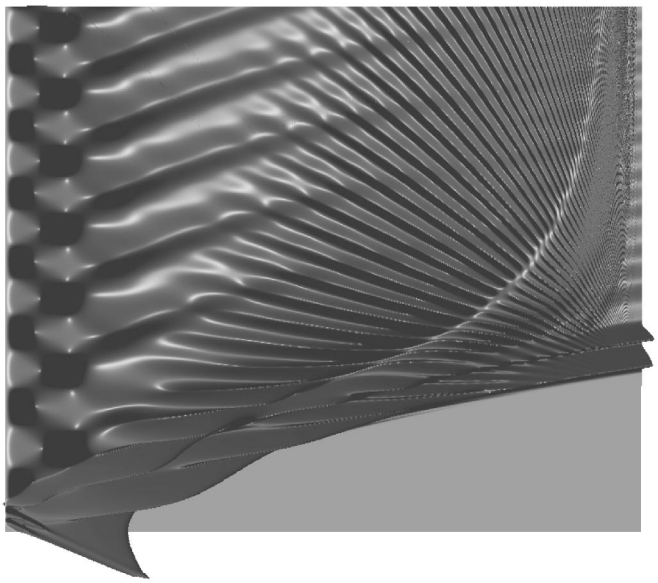

FIG. 14. The spacetime plot of the quantity $\mathcal{S}$ for the intermediate excitation with amplitude $c = 70$ for the space and time intervals $0 \le R \le 1$ and $0 \le T \le 2.885\,59$.

same characteristics of the evolution as on the previous figure, relevant for the large exciting pulse, show up clearly on this figure, as well.

By virtue of Fig. 14, at least two different phenomena clearly manifest themselves. First, the amplitude of the energy current density is much smaller beyond the shells of high frequency oscillations (this region is represented by the relatively smooth part close to the right vertical edge) than before reaching these shells. Actually, the "ribs," representing the maximal values of $\mathcal{S}$, apparently follow the shape of outgoing null rays all the way out to $\mathscr{I}^+$, but they are getting to be modulated more and more by the slowly moving massive shells of oscillations in the distance. Second, it is also apparent that some sort of inward directed energy transfer starts at the location where the ribs meet the massive shells of oscillations.

These shells of oscillations can be nicely pictured by focusing on a small subsection of the previous spacetime diagram as shown in Fig. 15.

Finally, we would like to attract attention to the appearance of some interesting features of the oscillations close to the origin. As the strength of the applied excitation is increased, the associated shapes, which can be clearly recognized on the following spacetime plots, are getting more and more complex. By virtue of Figs. 16–18, it is tempting to say that there might be a means of switching on more and more oscillating degrees of freedom of the monopole as the energy of the exciting pulse is increased. Notice that despite the relatively late time interval, the oscillating shapes are still present. Since $\mathcal{E} = \mathcal{E}_0 = 0$ at the left vertical edge corresponding to $R = 0$, it can be clearly seen from the figures that for the larger excitations the energy contained in the central region is definitely smaller than the energy contained in the same region of the static monopole. This means that at the center still there is a huge deficit in the energy, i.e. a considerably large fraction of the energy of the static BPS monopole is still somewhere in the outer region. A very large pulse in this sense almost destroys the monopole, scattering its energy

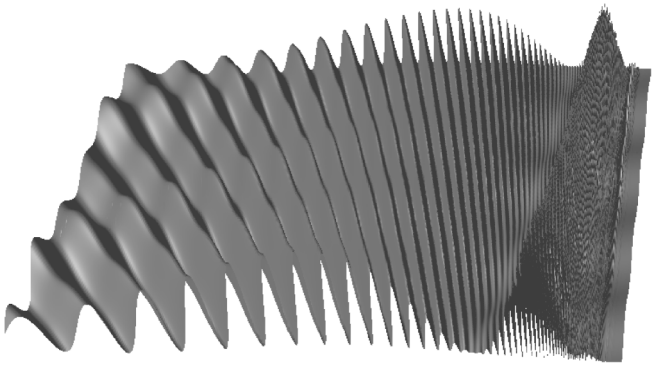

FIG. 15. The spacetime plot of the quantity $\mathcal{S}$ for the intermediate excitation with $c = 70$ for the space and time intervals $0.5829 \leq R \leq 1$ and $2.118\,64 \leq T \leq 2.885\,59$.

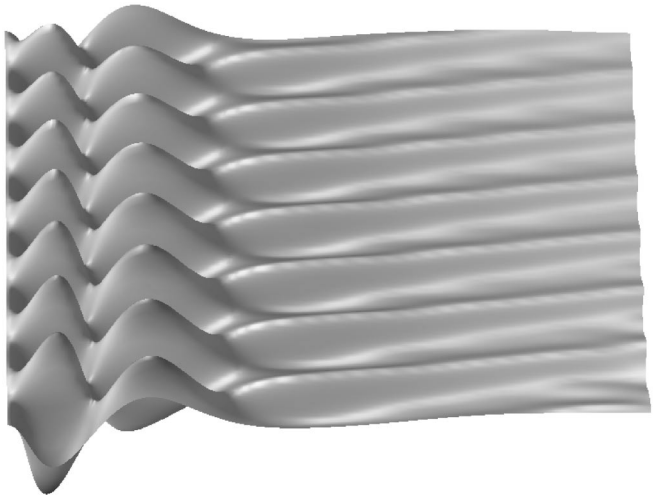

FIG. 16. The space and time dependence of $\mathcal{E} - \mathcal{E}_0$ for the intermediate excitation with amplitude $c = 70$ for the coordinate domain given by the relations $0 \leq R \leq 0.35$ and $1.695 < T < 4.237$.

to faraway regions. Of course, because of the charge conservation, this energy has to come back slowly to the center, forming the well-localized monopole again with smaller and smaller amplitude oscillations.

3. The space and time dependence of the pressure

There are two types of pressure, the radial and tangential, that can be associated with our spherically symmetric system. They are given as $P_{\mathrm{rad}} = T^{ab} n_a^{(R)} n_b^{(R)}$ and $P_{\mathrm{ang}} = T^{ab} n_a^{(\theta)} n_b^{(\theta)}$, respectively, where $n_a^{(R)}$ and $n_a^{(\theta)}$ denote the unit norm spacelike vector proportional to the coordinate differentials $(dR)_a$ and $(d\theta)_a$, respectively. The radial and tangential pressures are not equal to each other as may

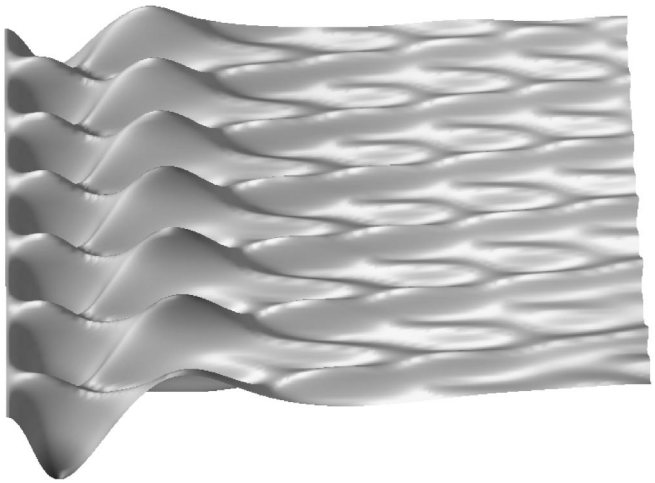

FIG. 17. The spacetime plot of $\mathcal{E} - \mathcal{E}_0$ for the large excitation with amplitude $c = 280$ for the space and time intervals $0 \leq R \leq 0.35$ and $1.695 \leq T \leq 4.237$. The maximum values are about 10 times larger than the those are in Fig. 16.

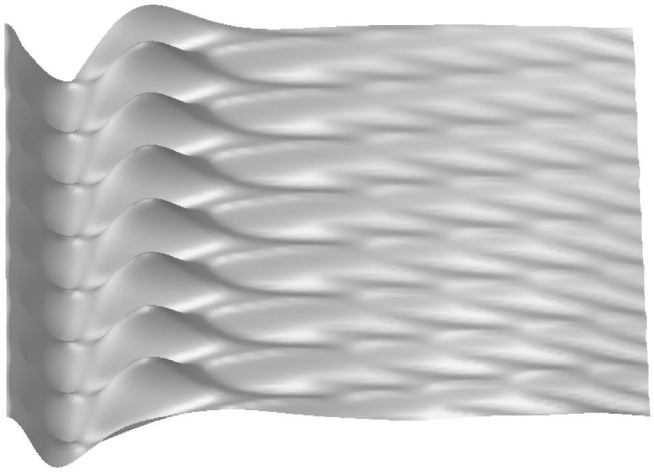

FIG. 18. The spacetime plot of $\mathcal{E} - \mathcal{E}_0$ for the extra large excitation with amplitude $c = 1120$ for $0 \leq R \leq 0.35$ and for a later time interval $36.441 \leq T \leq 38.983$. Here the maximum values are still more than 3 times larger than those in Fig. 16.

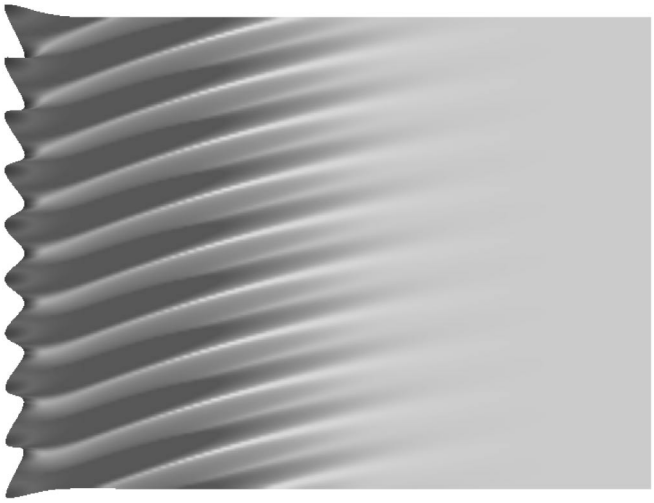

FIG. 20. The time evolution of the angular pressure P_{ang}. The system and the coordinate domain is exactly the same as in Fig. 19.

happen in the case of generic spherically symmetric configurations. Note that both of these pressures are identically zero for the static BPS configuration.

To be able to show the tiny features far form the center on these spacetime plots, in Figs. 19 and 20, we needed to multiply the pressures with an enormous scaling factor, and use an almost orthogonal projection (i.e. very faraway point of view) to compensate the scaling factor. Actually, the ratios of the values of the radial and angular pressure at the origin and at the middle of the plot, at $R = 0.5$, are about $1.5 \cdot 10^4$ and $2.3 \cdot 10^4$, respectively. This means that both of the pressures are significantly larger at the origin, where the monopole lives, than anywhere else.

It is clearly visible from Figs. 19 and 20 that there is a noticeable phase difference between the almost sinusoidal oscillations of the two pressures at the origin and somewhat more structured differences show up in the shape of the oscillations further away. Nevertheless, no really surprisingly new phenomenon, in addition to the formerly reported ones, can be observed on these figures.

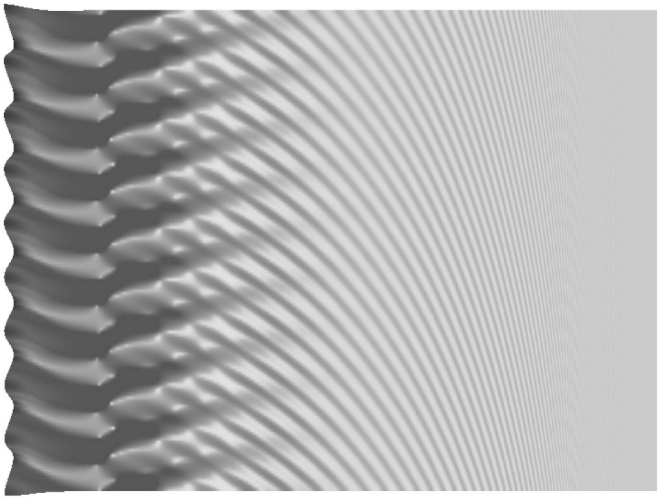

FIG. 19. The time evolution of the radial pressure P_{rad} for the intermediate exciting pulse with amplitude $c = 70$. The coordinate domain is given by the relations $0 \leq R \leq 1$ and $16.949 \leq T \leq 19.915$. Notice that this time period refers to that part of the evolution when the system behaves already much like a quasi-breather.

C. The quantitative picture

Before presenting a more detailed description of the behavior of the fundamental physical quantities let us show some simple but convincing results concerning the

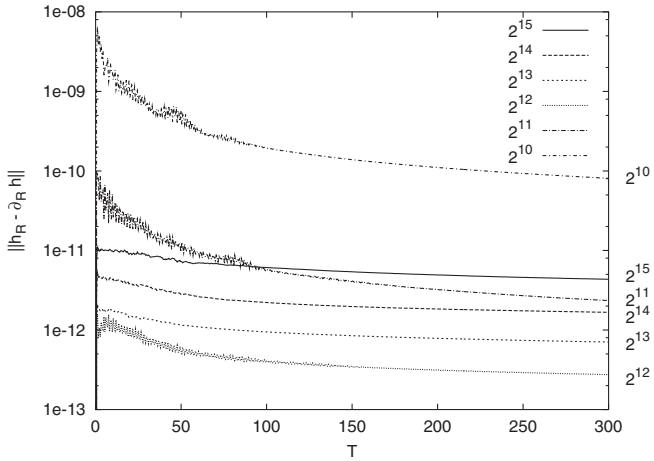

FIG. 21. Time dependence of the h constraint violation for several numerical resolutions corresponding to the indicated number of spatial grid points. The amplitude parameter in the initial data was chosen to be $c = 70$.

numerical preservation of the constraint equations during the investigated long term evolutions.

1. Monitoring of the constraints

Recall that the R derivatives of w and h are used as dependent variables, a consequence of which the relations $w_R = \partial_R w$ and $h_R = \partial_R h$ play the role of constraints now. In the analytic setting these relations are preserved by the evolution equations, provided that they hold on the initial surface. One of the possible tests of our numerical code is the monitoring of the violation of these constraints. In Fig. 21 the L^2 norm of the h constraint is presented as a function of time, defined as

$$||h_R - \partial_R h|| = \left(\int_0^1 (h_R - \partial_R h)^2 dR\right)^{1/2}. \quad (94)$$

It can be seen from the figure that for lower resolutions the error decreases when one increases the number of grid points. However, at higher resolutions, most likely because of rounding errors, the constraint violation becomes higher again. It is also apparent that apart from a short initial period the constraint violation is a decreasing function of time. The time dependence of the w constraint violation is similar to that of h on Fig. 21, only its magnitude is somewhat smaller.

Finally, we would like to emphasize that the numerical preservation of the constraint equations, reported above, in our rather long time evolutions is considerably good. Our code seems to be free, at least in the case of the investigated system, from the deficiencies of other approaches, where in the case of various dynamical systems exponential increase of the numerical violation of the constraint equations have been observed.

2. Energy balances

To monitor the appropriateness of the applied numerical scheme, we calculated energy balances for various spacetime domains. In particular, we considered the type of domains shown by Fig. 22 bounded by $T =$ const and $R =$ const hypersurfaces.

To see how the energy balances can be calculated, recall that whenever t^a is a Killing vector field, satisfying the Killing equation $\nabla^{(a} t^{b)} = 0$, the vector field

$$j^a = T^a_b t^b \quad (95)$$

is divergence free, i.e.

$$\nabla_a j^a = 0. \quad (96)$$

Then, by making use of Stokes's theorem, we have

$$\int_V \nabla_a j^a \boldsymbol{\epsilon} = \int_{\partial V} n_a j^a \tilde{\boldsymbol{\epsilon}} = 0, \quad (97)$$

where $\boldsymbol{\epsilon}$ denotes the 4-volume element while $\tilde{\boldsymbol{\epsilon}}$ is the 3-volume element induced on the boundary ∂V of V. Note

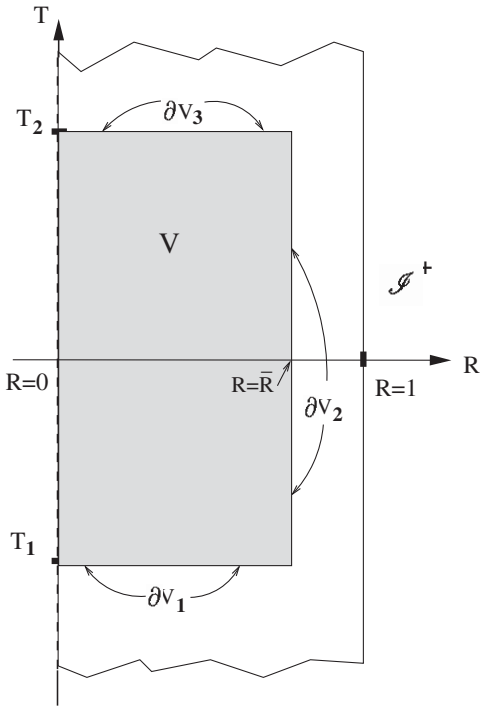

FIG. 22. The boundary $\partial V = \partial V_1 \cup \partial V_2 \cup \partial V_3$ of the shaded spacetime domain, represented by the union of the $T = T_1$, $T = T_2$, and $R = \bar{R}$ hypersurfaces.

that $\tilde{\boldsymbol{\epsilon}}_{abc} = n_e \boldsymbol{\epsilon}^e_{abc}$ where n_e is the (outward pointing) unit normal 1-form field on ∂V. For the following considerations we choose t^a as the unit norm static timelike Killing vector field $t^a = (\partial/\partial t)^a$.

Let us denote by $\mathcal{B}(\bar{T}, \bar{R})$ the ball of radius $R = \bar{R}$ centered at the origin of the $T = \bar{T}(=$ const) hypersurface; moreover, by $\mathcal{C}(T_2, T_1, \bar{R})$ the portion of the cylindrical hypersurface $R = \bar{R}$ between the $T = T_1$ and $T = T_2$ hypersurfaces. With these notations the boundaries, as indicated in Fig. 22, ∂V_1 and ∂V_3 are the balls $\mathcal{B}(T_1, \bar{R})$ and $\mathcal{B}(T_2, \bar{R})$, while ∂V_2 is the cylinder $\mathcal{C}(T_2, T_1, \bar{R})$ connecting them. Then the energy contained in a ball $\mathcal{B}(T, R)$ can be given as

$$E(T, R) = \int_{\mathcal{B}(T,R)} n^{(t)}_a j^a \tilde{\boldsymbol{\epsilon}}^{(t)}, \quad (98)$$

where $\tilde{\boldsymbol{\epsilon}}^{(t)}$ is the volume element on the constant T hypersurface and $n^{(t)}_a$ is its future pointing normal vector. Similarly, the energy transported through the timelike boundary $\mathcal{C}(T_2, T_1, R)$ is given as

$$S(T_2, T_1, R) = \int_{\mathcal{C}(T_2,T_1,R)} n^{(s)}_a j^a \tilde{\boldsymbol{\epsilon}}^{(s)}, \quad (99)$$

where $\tilde{\boldsymbol{\epsilon}}^{(s)}$ is the volume element on the constant R hypersurface and $n^{(s)}_a$ is its outwards pointing normal vector. Using these notations the energy balance Eq. (97) takes the form

$$E(T_2, R) - E(T_1, R) + S(T_2, T_1, R) = 0. \tag{100}$$

Note that while in analytic considerations the left-hand side of (100) is always identically zero, for any choice of T_2, T_1 and R, in meaningful numerical simulations the corresponding quantity is merely close to zero, i.e. an apparent violation of the energy conservation happens. In fact, the numerical value $N_{\rm vec}(T_2, T_1, R)$ of the "violation of the energy conservation" associated with a spacetime domain V, which is defined as

$$N_{\rm vec} = E(T_2, R) - E(T_1, R) + S(T_2, T_1, R), \tag{101}$$

can be used as one of the possible monitors of the appropriateness of a numerical code.

To evaluate the integrals (98) and (99) we need to determine the volume elements $\tilde{\boldsymbol{\epsilon}}^{(t)}$ and $\tilde{\boldsymbol{\epsilon}}^{(s)}$ which can be given as special cases of the relation

$$\tilde{\boldsymbol{\epsilon}}_{abc} = \sqrt{|g_{(4)}|}\varepsilon_{eabc}n^e, \tag{102}$$

where ε_{eabc} denotes the Levi-Civita alternating tensor with $\varepsilon_{0123} = 1$. To get $\tilde{\boldsymbol{\epsilon}}^{(t)}$ and $\tilde{\boldsymbol{\epsilon}}^{(s)}$, consider now the Minkowski spacetime in coordinates (T, R, θ, ϕ) associated with the applied conformal representation. Then the components $g_{\alpha\beta}$ of the metric tensor, g_{ab}, and its inverse read as

$$g_{\alpha\beta} = \frac{1}{\Omega^2}\begin{pmatrix} \frac{\Omega^2}{\kappa^2} & R & 0 & 0 \\ R & -1 & 0 & 0 \\ 0 & 0 & -R^2 & 0 \\ 0 & 0 & 0 & -R^2\sin^2\theta \end{pmatrix}, \tag{103}$$

and

$$g^{\alpha\beta} = \Omega^2\begin{pmatrix} \frac{4}{(R^2+1)^2} & \frac{4R}{(R^2+1)^2} & 0 & 0 \\ \frac{4R}{(R^2+1)^2} & -\frac{4\Omega^2}{(R^2+1)^2\kappa^2} & 0 & 0 \\ 0 & 0 & -\frac{1}{R^2} & 0 \\ 0 & 0 & 0 & -\frac{1}{R^2\sin^2\theta} \end{pmatrix}. \tag{104}$$

Calculating the determinant $g_{(4)}$ of the spacetime metric we obtain

$$\sqrt{|g_{(4)}|} = \frac{1}{2}\Omega^{-4}(R^2 + 1)R^2\sin\theta. \tag{105}$$

The future pointing normal form of $\mathcal{B}(T, R)$ has the components $n^{(t)}_\alpha = (1/\sqrt{g^{00}}, 0, 0, 0)$. This implies then that $n^{(t)0} = g^{00}n^{(t)}_0 = \sqrt{g^{00}} = \frac{2\Omega}{R^2+1}$; moreover, we have that

$$\tilde{\boldsymbol{\epsilon}}^{(t)}_{\alpha\beta\gamma} = \frac{R^2\sin\theta}{\Omega^3}\varepsilon_{0\alpha\beta\gamma} = \sqrt{|h^{(t)}|}(dR)_\alpha \wedge (d\theta)_\beta \wedge (d\phi)_\gamma, \tag{106}$$

where $h^{(t)}$ is the determinant of the three metric $h^{(t)}_{ab} = g_{ab} - n^{(t)}_a n^{(t)}_b$ induced by g_{ab} on $\mathcal{B}(T, R)$, i.e.

$$\sqrt{|h^{(t)}|} = \frac{R^2\sin\theta}{\Omega^3} \tag{107}$$

on $\mathcal{B}(T, R)$. Similarly, the normal of $\mathcal{C}(T_2, T_1, R)$, pointing out from the domain V, is $n^{(s)}_\alpha = (0, 1/\sqrt{-g^{11}}, 0, 0)$ and thereby $n^{(s)1} = g^{11}n^{(s)}_1 = -\sqrt{-g^{11}} = -\frac{2\Omega^2}{\kappa(R^2+1)}$ which implies, in particular, that

$$\begin{aligned}\tilde{\boldsymbol{\epsilon}}^{(s)}_{\alpha\beta\gamma} &= -\frac{R^2\sin\theta}{\kappa\Omega^2}\varepsilon_{1\alpha\beta\gamma} \\ &= \sqrt{|h^{(s)}|}(dT)_\alpha \wedge (d\theta)_\beta \wedge (d\phi)_\gamma,\end{aligned} \tag{108}$$

where $h^{(s)}$ is the determinant of the induced metric $h^{(s)}_{ab} = g_{ab} + n^{(s)}_a n^{(s)}_b$, and

$$\sqrt{|h^{(s)}|} = \frac{R^2\sin\theta}{\kappa\Omega^2}. \tag{109}$$

Taking the above relations into account, we get that

$$E(T, R) = \int_0^R \mathcal{E}(T, R')\mathrm{d}R', \tag{110}$$

$$S(T_2, T_1, R) = \int_{T_1}^{T_2} \mathcal{S}(T, R)\mathrm{d}T, \tag{111}$$

where $\mathcal{E}$ and $\mathcal{S}$ are the functions defined in (92) and (93).

In Figs. 23 and 24 the time dependence of the violation of the energy conservation $N_{\rm vec}(0, T, R)$ is shown for numerical runs with various resolutions evolving from initial data with amplitude $c = 70$. It can be seen from these figures that the error in the energy conservation decreases according to expected fourth order convergence during an initial period up to approximately $T = 0.7$ and also later, after $T > 20$. In the intermediate region the conservation

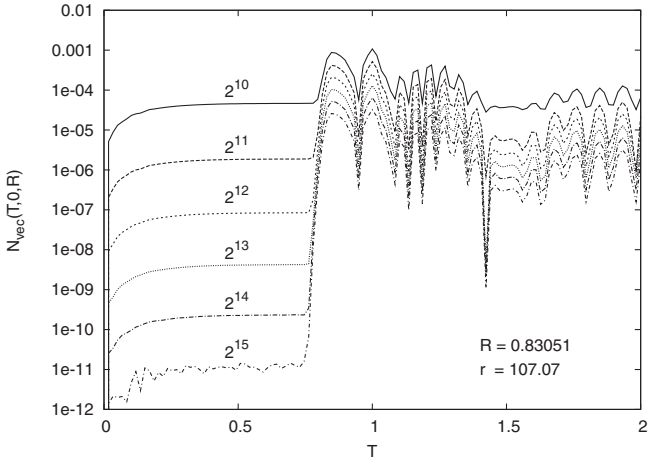

FIG. 23. Initial behavior of the numerical violation of the energy conservation $N_{\rm vec}(T, 0, R)$ for different spatial resolutions. The spacetime domain is bounded by the constant time surfaces $T_1 = 0$ and $T_2 = T$, while the cylindrical boundary is at $R = 0.83051$, corresponding to $r = 107.07$.

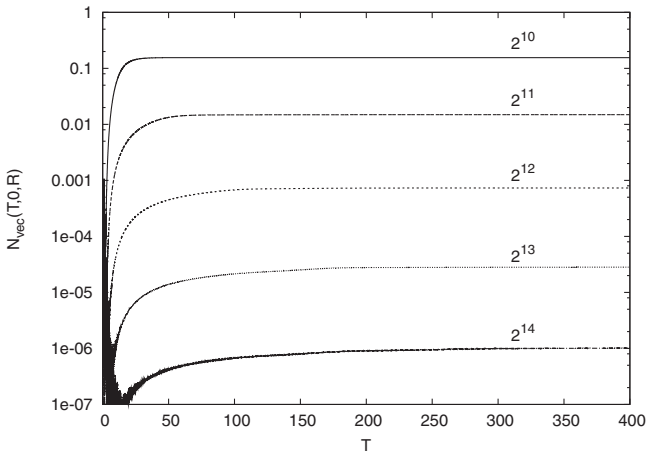

FIG. 24. The time dependence of the violation of the energy conservation $N_{\rm vec}(T, 0, R = 0.83051)$ for the same numerical simulations as on the previous figure but for a much longer time interval.

violation decreases more slowly. This is possibly due to the highly oscillating character of the fields in that time interval, especially since the energy current integrals were calculated only with a second order convergent method.

The magnitude of the presented constraint violations is really meaningful only if it can be compared to the full energy content. The time dependence of the difference $E(T, R) - E_s(R)$ of the dynamical and static energy functions, $E(T, R)$ and $E_s(R)$ is shown logarithmically on Fig. 25 for increasing numerical resolutions. For the chosen radius $R = 0.830\,51$, the energy of the static background monopole is $E_s(R) = 12.449$, less than double of the energy provided by the initial deformation. The convergence of the presented curves provides us a strong indication of how long we can take our numerical results seriously. For the highest resolution used, i.e. that with 2^{15} spatial grid points, the calculation becomes unreliable after

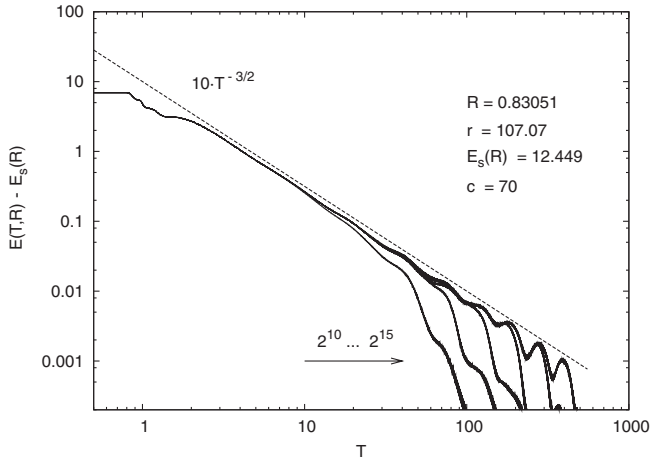

FIG. 25. Time dependence of the extra energy content $E(T, R) - E_s(R)$ plotted using logarithmic axes.

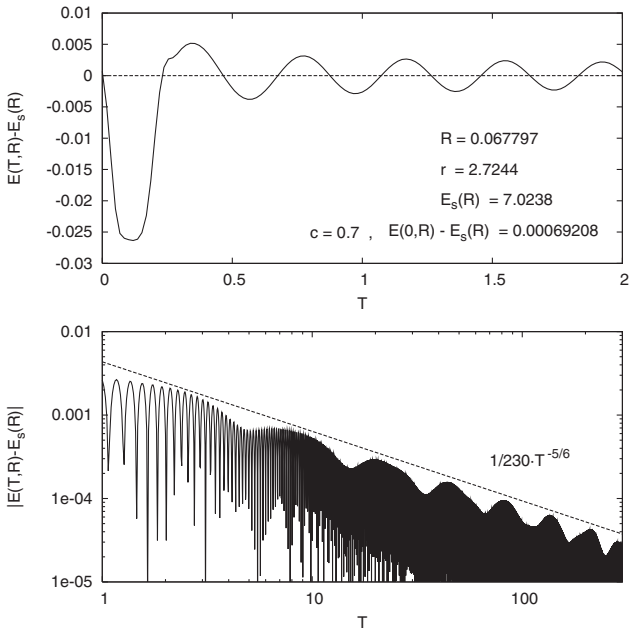

FIG. 26. The extra energy $E(T, R) - E_s(R)$ as a function of time contained inside radius $R = 0.067\,797$ for initial and longer time period, $1 \le T \le 300$. By careful analysis it can be justified that on average the energy content close to the origin might be slightly lower than that of the static monopole. The forming of a long-lasting breathing phase with a clear asymptotic time dependence can also be clearly recognized.

$T = 300$. We note that in physical time, i.e. in time measured in mass units, the time interval $\Delta T = 300$, at the center, corresponds to $\Delta t = 6000$, while the central monopole performs nearly 1000 oscillations.

3. Linear and nonlinear effects

In order to distinguish linear and nonlinear effects in the evolution of magnetic monopoles, we first present results corresponding to very small initial deformation, with amplitude $c = 0.7$. Then the extra energy provided by the initial pulse is only $0.000\,696\,595$, which is very small compared to the energy of the static monopole, which is $12.566\,37$ to seven digits precision. In Fig. 26, the time dependence of the extra energy is presented in a ball of radius $R = 0.067\,797$, which corresponds to $r = 2.7244$. Inside this radius the static background solution contains energy $E_s(R) = 7.0238$, which is about 56% of the total energy of the static monopole. For this low energy case, after a short initial period, the energy content starts oscillating around the energy of the static monopole. The time decay of these oscillations is $T^{-5/6}$ to a good approximation. In Fig. 27 the energy content is presented in a much larger ball, with radius $R = 0.830\,51$, corresponding to $r = 107.07$. Inside this large radius the energy contained in the static monopole is 12.449, which is 99% of the total static energy. It is apparent that, because the Yang-Mills field is massive, part of the energy provided by the pulse

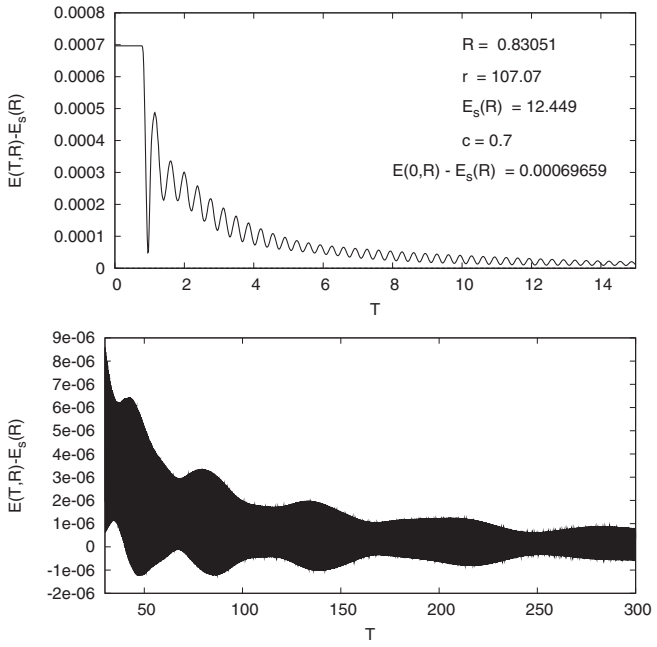

FIG. 27. The extra energy content $E(T, R) - E_s(R)$ for radius $R = 0.830\,51$ in case of the low energy deformation, with $c = 0.7$. It is transparent that, although the energy content close to the origin might be slightly lower than that of the static monopole, up to this relatively large radius the system possesses more energy on the average than the static monopole had.

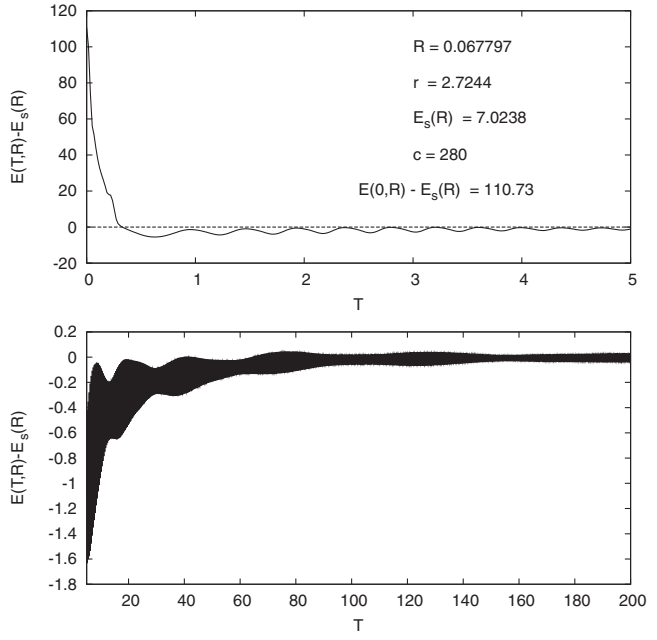

FIG. 28. The extra energy content $E(T, R) - E_s(R)$ for radius $R = 0.067\,797$ for high energy deformation corresponding to $c = 280$. The graphs clearly indicate that for a large exciting pulse the average energy content of the central region is below that of the static monopole.

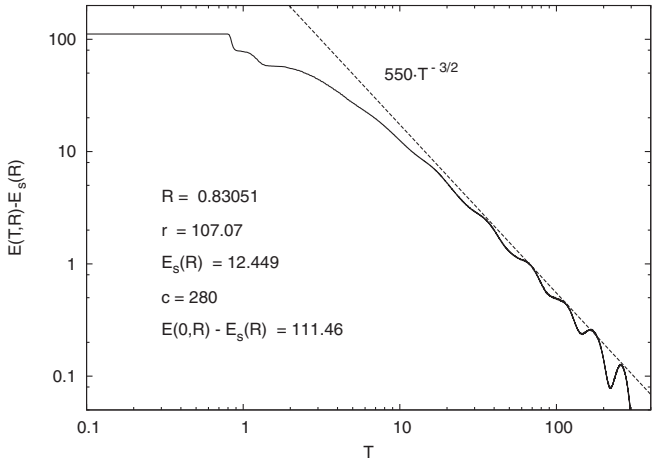

FIG. 29. The extra energy content $E(T, R) - E_s(R)$ for the larger radius $R = 0.830\,51$ and for the high energy deformation with $c = 280$. The asymptotic power law time decay can easily be read off the *log scale* plot.

remains inside this radius for quite a long time. The oscillations of the energy content will be centered around the static value only after about $T > 100$.

In Fig. 28 the energy contained in the same small radius $R = 0.067\,797$ as the one used in Fig. 26 is shown for a large initial deformation corresponding to $c = 280$. In this case the energy provided by the pulse inside this radius is 110.73, which is about 15 times more than the energy of the static monopole in this region. The main difference compared to the previous case is that the oscillation of the energy is not centered on the static monopole energy anymore. The average value of the energy is below the static value for a very long time period. We interpret this as a nonlinear effect. The expanding initial pulse sweeps out not only the provided extra energy but also a part of the energy of the static monopole. It takes a long time to get back this energy which is stored in the massive Yang-Mills field oscillations at intermediate distances from the monopole. In Fig. 29 the extra energy is shown for the same large initial pulse but for the larger radius, $r = 107.07$. Inside this large radius, just like in the case of the tiny excitation with $c = 0.7$ (see Fig. 26), the energy remains above the static value during the entire evolution where our numerical simulation can be considered to be valid.

In Fig. 30, the effect of an extra large initial pulse is presented. In this case the amplitude of the initial pulse was chosen to be $c = 1120$, corresponding to provided energy 1771.75 inside the $R \leq 0.067\,797$ region. In this case the initial pulse quickly sweeps out most of the energy of the monopole from the central region. However, after some highly energetic oscillations, the major part of the monopole energy returns, and the energy content starts to oscillate around a value below that of the static monopole, like in the case of the less energetic nonlinear excitations considered previously.

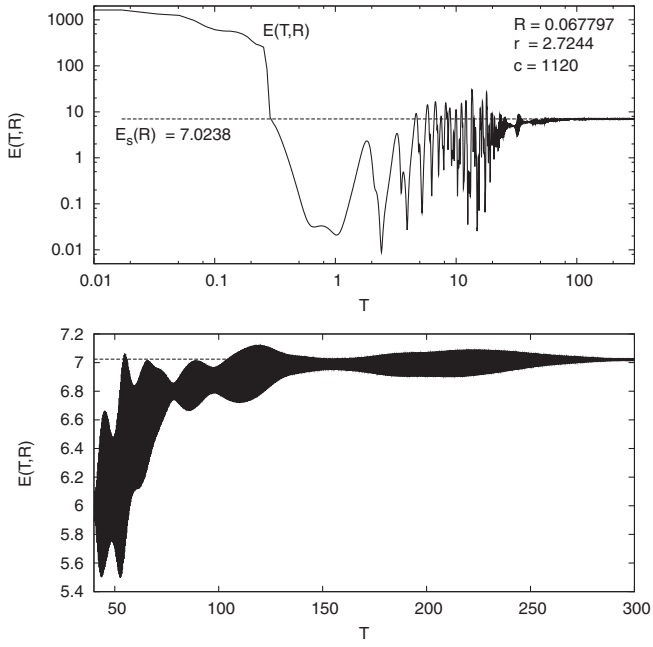

FIG. 30. The full energy content $E(T, R)$ inside radius $R = 0.067\,797$ for an enormously large initial pulse with $c = 1120$. Even though the monopole seems to be swept out from the central region for the initial period, eventually the behavior of the system returns to an oscillating normal monopole state.

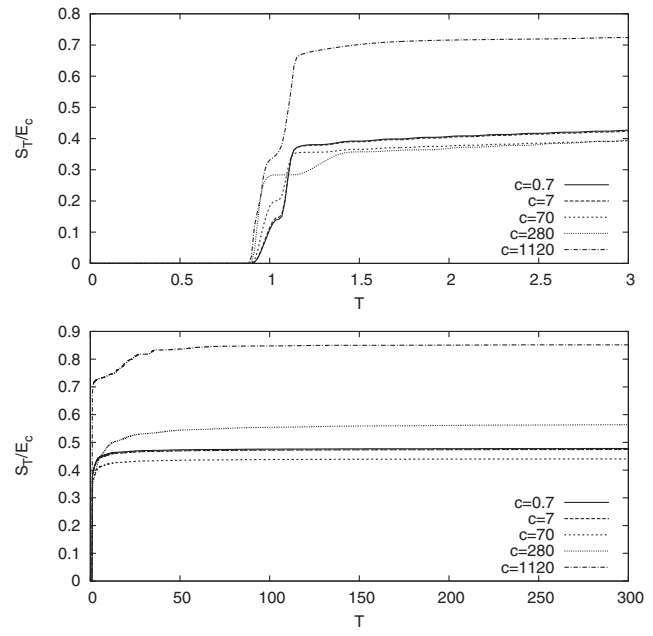

FIG. 31. The ratio S_T/E_c is plotted for five different choices of the initial amplitude c, where $S_T = S(T, 0, 1)$ is the energy radiated to infinity up to T and E_c denotes the energy provided by the exciting pulse.

4. The time dependence of the total radiated energy at $\mathscr{I}^+$

In this subsection we provide a short account on the time dependence of the energy radiated to future null infinity. Since the Yang-Mills field is massive, w decays exponentially when approaching the $R = 1$ line corresponding to null infinity. This implies that the intensity of the radiation to $\mathscr{I}^+$ is determined only by h and its first derivatives at $R = 1$. The full radiated energy up to the moment T, i.e. $S_T = S(T, 0, 1)$ in terms of the notation introduced in Sec. VII C 2, depends on the amount of energy E_c provided by the initial deformation (91). For our special choice of initial data, E_c is proportional to c^2. In Fig. 31 the ratio S_T/E_c is plotted for five different initial data amplitudes. It can be seen that except for very large initial energies, the radiated energy is closely proportional to the energy contained in the initial pulse. In Table I, for the five chosen c amplitude values, we list the energy of the initial pulse E_c, its ratio to the energy of the static monopole E_c/E_s, the fraction of the initial energy radiated up to $T = 300$, and the fraction of the initial energy radiated during the whole time evolution. The value S_∞ was estimated by assuming that the energy content of the system decreases according to a power law decay with $T^{-3/2}$ during the later stages of the radiation process. As it can be seen in Figs. 32 and 33, this is certainly a very good approximation for weaker initial excitations, and it appears to be consistent with the late time behavior of more energetic evolutions.

Notice that since $S_\infty < E_c$, the limit of the energy associated with the system, on $T = \text{const}$ hypersurfaces, *does not* tend to the energy of the original BPS monopole. This observation is in fact in accordance with the existence of the massive shells of high frequency oscillations. These shells never reach future null infinity, and hence they store for the rest of the entire evolution a part of the energy of the original exciting pulse. This phenomenon gets to be even more transparent if one thinks of a simple massive Klein-

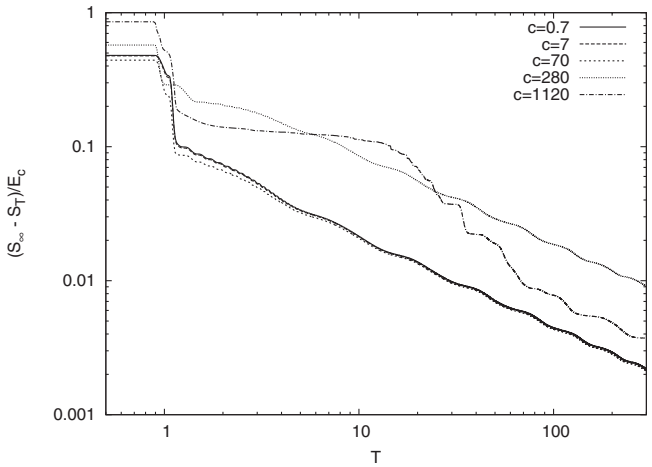

FIG. 32. The quantity $(S_\infty - S_T)/E_c$ is plotted logarithmically for the indicated values of the initial amplitude c.

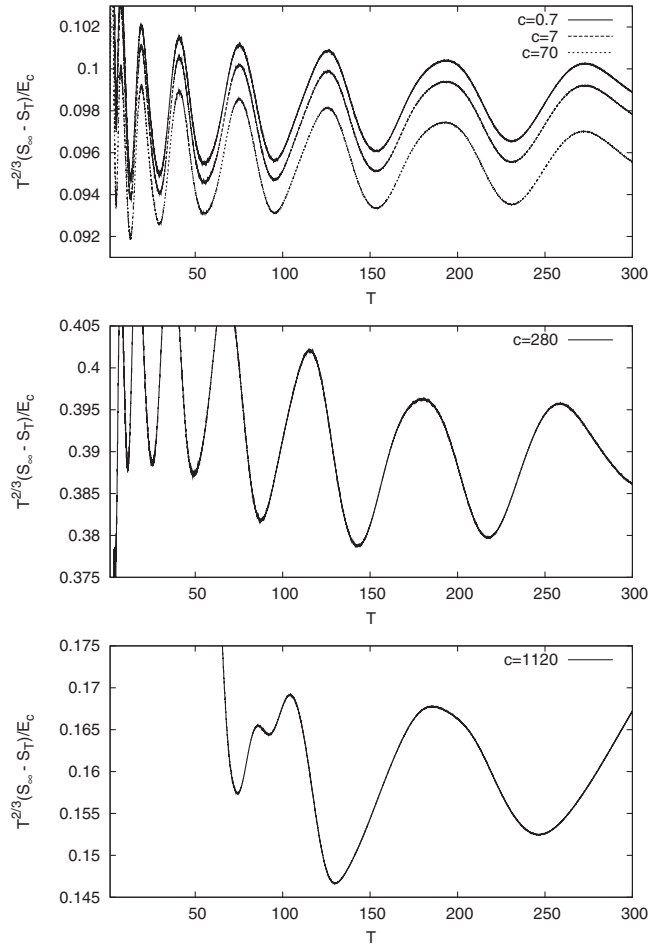

FIG. 33. The quantity $(S_\infty - S_T)/E_c$ multiplied by $T^{2/3}$ for the five different initial data configurations.

Gordon system starting, say, from a trivial configuration where only the exciting pulse stores energy. The pulse disperses, as it is expected, but the system is conservative so the total energy has to be conserved. Due to this, there is no upper bound on the increase of the frequency associated with these shells of oscillations forming even in this simplest possible linear case. Let us mention that a more detailed discussion of this phenomenon can be found in [4].

5. The space and time dependence of the energy transfer towards $\mathscr{I}^+$

One of the possible methods in monitoring the main features of the energy transfers is to investigate in more detail the space and time dependence of the extra energy content of the dynamical monopole. Figure 34 pictures the time dependence of the difference $\Delta E = E(T, R) - E_s(R)$ along the constant R slice, with $R = 0.1949$, corresponding to $r = 8.1045$. In particular, on the upper part of the figure the time dependence of ΔE, along with its maximum and minimum contours, together with the associated average or mean value, are plotted for the time interval $2 \leq T \leq 17$. Notice that, even in the case of the considered intermediate excitation, at the indicated relatively long time period the mean value of the difference $E(T, R) - E_s(R)$ is still negative. Looking at this plot it is also clear

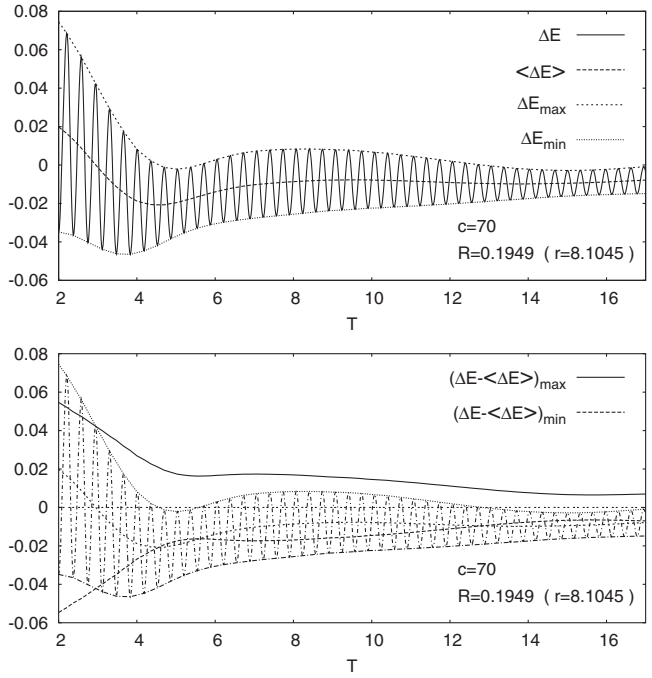

FIG. 34. Upper plot: the difference $\Delta E = E(T, R) - E_s(R)$, along with the maximum, minimum contours and the mean values, for the time interval $2 \leq T \leq 17$. Lower plot: the maximum, minimum contours associated with the separated high frequency oscillations, i.e., with $\Delta E - \langle\Delta E\rangle$, where $\langle\Delta E\rangle$ denotes the mean value of the difference $\Delta E = E(T, R) - E_s(R)$.

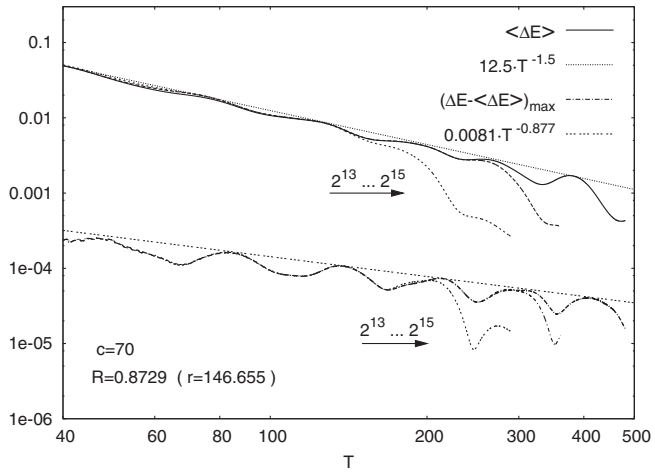

FIG. 35. The convergence in the *log-log* plots of ΔE and $(\Delta E - \langle\Delta E\rangle)_{\max}$ along the R slice with $R = 0.8729$ and for the time interval $40 \leq T \leq 500$. This *log-log* plot clearly manifests also the power law decay of the amplitude of the high frequency oscillations $(\Delta E - \langle\Delta E\rangle)_{\max}$ and that of the mean value $\langle\Delta E\rangle$ with the particular values $\alpha = 0.877$ and $\mu = 1.5$.

that the time dependence of the amplitude of the high frequency oscillations and that of the mean value should be investigated separately. For this purpose we investigated separately the time dependence of the mean value $\langle \Delta E \rangle$, and the time dependence of the amplitude of the high frequency oscillations $(\Delta E - \langle \Delta E \rangle)_{\max}$. In the lower part of Fig. 34 the behavior of these separated variables are shown for the same time period as on the upper graph.

By making use of *log-log* plots, see e.g. Fig. 35, for various R slices it is again straightforward to recognize a power law time decay that can be associated with both the amplitude of the high frequency oscillations, $(\Delta E - \langle \Delta E \rangle)_{\max}$, and that of the mean value, $\langle \Delta E \rangle$. In particular, denoting by $-\alpha$ and $-\mu$ the two power law exponents, we have that $\langle \Delta E \rangle \sim T^{-\mu}$ and $(\Delta E - \langle \Delta E \rangle)_{\max} \sim T^{-\alpha}$, respectively.

Table II collects more information about the R dependence of the values of the power law decaying exponents α and μ in case of excitation with $c = 70$. Apparently there is a certain universality in the dying out of the high frequency oscillations, where the numerical value of α is very close to $5/6$. Nevertheless, contrary to our expectations, it turned out that the time dependence of the mean value $\langle \Delta E \rangle$ reflects some sort of nonuniversal features, i.e., the value of μ varies, so it is, in general, different from 1.5 which had been associated with the $R = 0.8305$ slices in case of the excitations with amplitudes $c = 70$ and $c = 280$ (see Figs. 25 and 29).

It is important to emphasize that by the mere nature of the applied approximations, there is no numerical method which could represent the full history of the expanding shells of high frequency oscillations properly. Therefore, it is of distinguished importance to know how strongly the above reported results, concerning the energy transport, depend on the applied numerical resolution. Is there at all a meaningful convergence guaranteed, say, at a suitably large value of R close to the region occupied by the shells of high frequency oscillations? Figure 35 is to justify that for the largest value of R referred to in Table II, i.e. at the $R = 0.8729$ slice, such a convergence is guaranteed by our numerical method.

TABLE II. The asymptotic time dependence of $\langle \Delta E \rangle$ and $(\Delta E - \langle \Delta E \rangle)_{\max}$, along $R = \text{const}$ slices, were found to follow the power law time decay $\langle \Delta E \rangle \sim T^{-\mu}$ and $(\Delta E - \langle \Delta E \rangle)_{\max} \sim T^{-\alpha}$, respectively. This table provides the values of μ and α for the indicated R slices in case of excitation with $c = 70$.

r	R	μ	α
1.0176	0.0254	0.9	0.833 33
2.7244	0.0678	0.94	0.833 33
4.4609	0.110 169	0.9	0.828
6.2471	0.1525	0.87	0.833
8.1045	0.1949	0.86	0.83
13.232	0.3010	1.2	0.8333
19.497	0.4068	1.5	0.833 33
27.822	0.5127	1.52	0.833
40.088	0.6186	1.54	0.8333
61.018	0.7246	1.55	0.833
107.074	0.8305	1.53	0.84
146.655	0.8729	1.5	0.877

It is important to interpret the above findings in short physical terms. For instance, Table II clearly justifies that there is an inner region with a certain type of universal time decay for the mean value of the extra energy content which can be characterized by the value $\mu \sim 0.86$–0.9. Essentially, this region corresponds to the core of the monopole. Since the value of μ is the smallest in this inner region, the energy transfer remains at a much higher level here for the entire evolution. It is also interesting that the value of μ is smaller a bit apart from the center than close to the center which indicates that there remains some energy bouncing back and forth during the entire evolution in the central region where the monopole lives. Then, there is a wide region at the middle, characterized by the interval $0.3 \leq R \leq 0.87$, where the mean value of the extra energy content is decaying more rapidly than elsewhere. Notice that the increase of the exponent μ from about $R = 0.3$ till $R = 0.72$ with the increase of the value of R indicates that a larger and larger fraction of the extra energy provided by the exciting pulse is stored by the expanding shells of high frequency oscillations of the Yang-Mills field. In fact, this conclusion is also supported by the slower and slower time decay as the value of R is further increased above $R = 0.72$.

Let us finally investigate the energy content stored in expanding shells of high frequency oscillation formed by the massive Yang-Mills field represented by w at large radii. The energy content outside of $\bar{R}$ is $E(T, 1) - E(T, \bar{R})$. Since initially the energy contained in this region is $E_s(1) - E_s(\bar{R})$, the energy stored in the shells is

$$E_{\text{shells}} = E(T, 1) - E(T, \bar{R}) - [E_s(1) - E_s(\bar{R})], \quad (112)$$

which can be written as

$$E_{\text{shells}} = [E(T, 1) - E(\infty, 1)] - [E(T, \bar{R}) - E_s(\bar{R})] + [E(\infty, 1) - E_s(1)]. \quad (113)$$

Recall (see Sec. VII C 4) that the mean value of the total energy $E(T, 1)$ associated with $T = \text{const}$ slices is approaching its nonzero limit value $E(\infty, 1)$ by following a time decay of the form $T^{-2/3}$. As it can be seen from Table II, the second term on the right-hand side of (113) always dies out faster than the first one. This relation justifies that the energy stored by the shells of high frequency oscillations has to approach asymptotically the positive value $E(\infty, 1) - E_s(1)$ from above with the power law decay $\sim T^{-2/3}$.

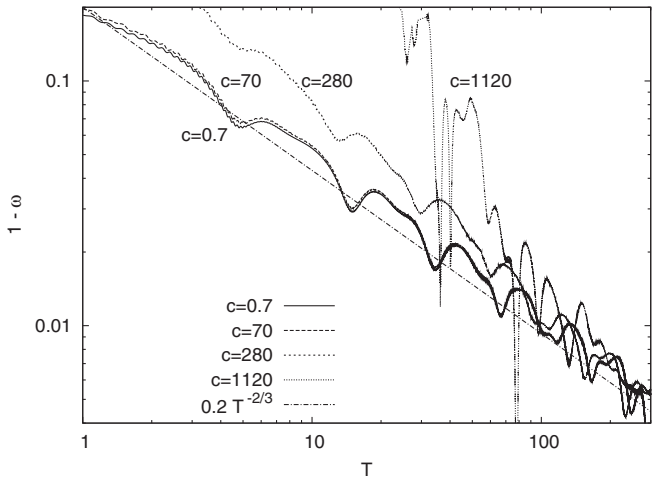

FIG. 36. Time dependence of the oscillation frequency ω of the field w at $R = 0.025\,42$, i.e. at $r = 1.017$, for four different initial data labeled by the strength parameter c. Since the frequencies approach 1 from below, the value of $1 - \omega$ is plotted logarithmically. The evolution of the frequency for the weak ($c = 0.7$) and intermediate energy ($c = 70$) excitations tends as $T^{-2/3}$ to the limit value 1. For the higher energy simulations, $1 - \omega$ falls off more quickly. For the $c = 1120$ simulation the downwards pointing peaks correspond to moments where the frequency approaches 1 closely from below and then gets smaller again.

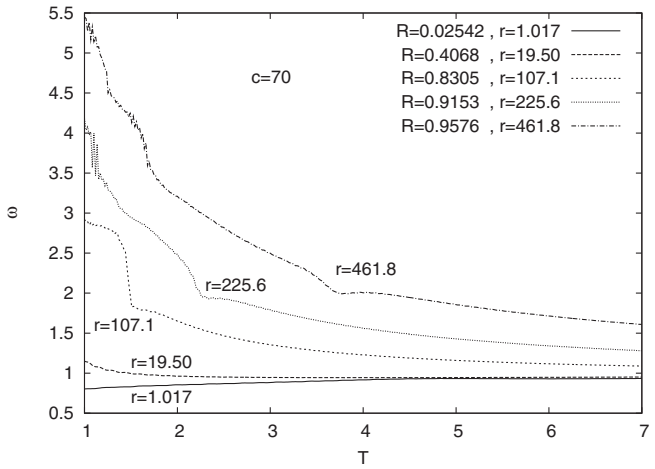

FIG. 37. Time dependence of the frequency of the oscillation of the w field at five different constant radii for a shorter time interval, $1 \le T \le 7$. The parameter in the initial data was chosen to be $c = 70$. Outside the core of the monopole the frequency decreases from a peak value reached before $T = 1$. Although the $T < 1$ region is not shown because of the high error of our frequency determination method there, the frequency reaches at least $\omega = 10$ for the early stages at larger radii.

6. The time dependence of the frequency of oscillations

The time dependence of the frequency of the massive w and massless h fields display markedly different characteristics. Frequency dependence of composite quantities such as the energy density will show a mixture of these properties. As can be seen on Figs. 9 and 11, the behavior of the Higgs field h is essentially the same at each radius R, apart from a slowly increasing phase shift going outwards. But even this time delay is not very significant, since this change is along outgoing null geodesics. A null geodesic emanating from the center $R = 0$ reaches null infinity $R = 1$ in a coordinate time interval $\Delta T = 1$, which is small compared to the length of the simulations performed by our numerical code. The behavior of the w field is qualitatively different, as it is apparent from Figs. 8 and 10. In the central region, the two fields are strongly coupled and consequently their frequency is the same. In Fig. 36 the time dependence of the frequency of the w field is shown for four different initial data at a fixed radius $R = 0.025\,42$, corresponding to $r = 1.017$. The time dependence of the h field at this radius would yield an essentially identical figure.

The difference between the frequency evolutions of the w and h fields gets manifested at higher radii, far from the core of the magnetic monopole. At these distances expanding shell structures appear in w, oscillating with high frequencies. We know by virtue of the results of [4] that at a given radius R the frequency of these shells is the highest just after direct outgoing geodesics emanating from the initial perturbation region of the $T = 0$ initial hypersurface reach out to the coordinate radius R. Of course, because of the high coordinate velocity of the outgoing null rays, this happens before $T = 1$. It is an interesting result of [4] that if R approaches 1 then the highest frequency increases without any bound. After the highest frequency expanding shells have left the radius R, the frequency is decreasing steadily, until it falls to a minimum value below

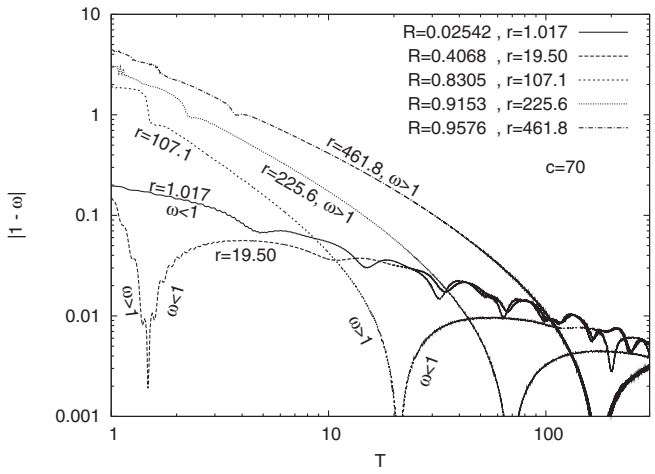

FIG. 38. Time dependence of the frequency for the same system and same choice of radii as on the previous figure, but for a longer time interval, $1 \le T \le 300$. Since the frequencies tend to 1, the absolute value of $1 - \omega$ is plotted logarithmically. The downward pointing peaks correspond to moments where ω falls below 1. This happens later for larger radii.

1, and then starts to approach 1 from below, more or less according to the $T^{-2/3}$ law observed in the central region. The time evolution of the frequency of the w field for an initial excitation with $c = 70$ is shown at five different radii on Figs. 37 and 38.

7. The magnetic charge

It is known that in a gauge theory, like the one considered in this paper, by making use of the formal definition applied in Maxwell theory, a conserved magnetic charge can be defined although the yielded charge is a Lie-algebra-valued quantity. Hence a meaningful definition of magnetic charge requires the use of a gauge independent specification of what is considered to be the ''electromagnetic content'' of the system.

Historically two main approaches developed. The first one was suggested by 't Hooft [23]. It is based on the use of the gauge independent expression [37]

$$\mathcal{F}_{ab} = \frac{1}{|\psi|}\,\mathrm{tr}(\psi F_{ab}) + \frac{i}{g|\psi|^3}\,\mathrm{tr}(\psi[D_a\psi, D_b\psi]), \quad (114)$$

where $|\psi| = \mathrm{tr}(\psi\psi)^{1/2}$. It can be checked that in terms of the variable $\mathcal{A}_a = \frac{1}{|\psi|} tr(\psi A_a)$ the above ''Maxwell'' tensor can be given as

$$\mathcal{F}_{ab} = \partial_a \mathcal{A}_b - \partial_b \mathcal{A}_a. \quad (115)$$

Note, however, that in spite of the elegance of this construction the main drawback is that according to this definition the magnetic charge can reside only at the zeros of the Higgs field, which means that in our case the magnetic charge has to be pointlike; it is concentrated to the origin.

According to a general expectation the 't Hooft-Polyakov magnetic monopole has the preferable property of being nonsingular in contrast to the Dirac monopole (see e.g. [24]). A proposal, made by Polyakov and Fadeev, fitting to this desire, which will also be applied in the rest of this section, is given by the simple relation [15]

$$\mathcal{F}_{ab} = \frac{1}{H_0}\,\mathrm{tr}(\psi F_{ab}), \quad (116)$$

where H_0 is the vacuum expectation value of the Higgs field [see Eq. (3)].

This section is to provide a brief account on the associated definition of the time- and location-dependent magnetic charge density and the conserved total magnetic charge. Note that in the case of the applied minimal dynamical generalization of the static t' Hooft-Polyakov magnetic monopole no electric charge or electric charge density are generated. However, in more generic considerations, involving all the physical degrees of freedom, associated with e.g. the most general spherically symmetric excitations of the BPS magnetic monopole, nontrivial electric charge density appears, although the vanishing of the total electric charge is guaranteed [10].

Analogous to the arguments applied in Maxwell theory, the magnetic charge density can be calculated by making use of the magnetic field strength

$$B_a = -\tfrac{1}{2}\epsilon_{abcd} u^b \mathcal{F}^{cd}, \quad (117)$$

which is defined with respect to a family of observers represented by a timelike unit norm 4-velocity field u^a. The magnetic charge density is given then as the 3-divergence of B_a

$$\rho^M = \tilde{\nabla}^e B_e, \quad (118)$$

where $\tilde{\nabla}_a$ denotes the covariant derivative operator associated with the 3-metric induced on the 3-space ''orthogonal'' to the 4-velocity field u^a.

To be more specific and precise, let us choose the timelike unit 4-vector field u_a to be everywhere normal to the $T = \text{const}$ hypersurfaces. Then, for the components of u_a

$$u_\alpha = \left(\frac{1}{\sqrt{g^{TT}}}, 0, 0, 0\right) \quad (119)$$

holds, while the induced metric on the $T = \text{const}$ hypersurfaces can be given as

$$h_{ab} = g_{ab} - u_a u_b. \quad (120)$$

Notice that for any fixed value of T the vector field u^a coincides with the timelike unit norm $n^{(t)a}$ introduced in the previous section.

Carrying out all the necessary calculations and combining all the above relations we get that

$$B_R = -\frac{\Omega}{gR^2}\frac{H}{H_0}(1 - w^2). \quad (121)$$

Moreover, the expression of the magnetic charge density ρ^M simplifies to the relation

$$\rho^M(T, R) = \frac{\Omega^3}{gH_0R^2}\,\partial_R(H[1 - w^2]), \quad (122)$$

where, by virtue of (28) and (36), the function H stands for the expression $H = h\Omega/R + H_0$. It is important to note that in the smooth setting, the function $\partial_R(H[1 - w^2])$ vanishes up to second order in a small neighborhood of the origin, i.e. there exists a smooth function $\varphi = \varphi(T, R)$ so that $\partial_R(H[1 - w^2]) = \varphi R^2$. This, however, guarantees that the magnetic charge density ρ^M is regular at the center as it was anticipated.

Let us define, again referring to analogies from Maxwell theory, the magnetic charge associated with a region $\mathcal{V}$ in a spacelike hypersurface Σ by the integral

$$\mathrm{Q}^M(\mathcal{V}) = \int_{\mathcal{V}} \tilde{\epsilon}\rho^M, \quad (123)$$

where now $\tilde{\epsilon}$ denotes the 3-volume element of the spacelike hypersurface Σ.

Returning to the previously used specific choice, let us choose $\mathcal{V}$ to be the ball of radius R centered at the origin on a $T = \text{const}$ hyperboloidal hypersurface, i.e. $\mathcal{V} = \mathcal{B}(T, R)$. Notice, that according to (120) the components of the 3-volume element $\tilde{\epsilon}$ takes the form given by the relation (106). Moreover, by virtue of the Stokes theorem and (118) the magnetic charge associated with the region $\mathcal{B}(T, R)$ can be given as a surface integral on the boundary of $\mathcal{B}(T, R)$

$$\mathrm{Q}^M(T, R) = \int_{\mathcal{B}(T,R)} \tilde{\nabla}^e B_e \tilde{\epsilon} = \int_{\partial\mathcal{B}(T,R)} \nu^e B_e \hat{\epsilon}, \quad (124)$$

where ν^a denotes the outward pointing spacelike unit normal field on the boundary $\partial\mathcal{B}(T, R)$ of the region $\mathcal{B}(T, R)$, while $\hat{\epsilon}$ is the volume element associated with the induced metric χ_{ab} on $\partial\mathcal{B}(T, R)$ which is given as

$$\chi_{ab} = h_{ab} + \nu_a \nu_b. \quad (125)$$

Since the outward pointing unit normal field ν^a in the considered special case is proportional to $(\frac{\partial}{\partial R})^a$, we have for the components of ν^a that

$$\nu^\alpha = \left(\frac{1}{\sqrt{-h_{RR}}}, 0, 0\right), \quad (126)$$

and hence, also that

$$\chi_{\alpha\beta} = \frac{1}{\Omega^2}\begin{pmatrix} -R^2 & 0 \\ 0 & -R^2\sin^2\theta \end{pmatrix}, \quad (127)$$

which leads to the relation

$$\hat{\epsilon}_{\alpha\beta} = \frac{R^2\sin\theta}{\Omega^2}\varepsilon_{01\alpha\beta} = \sqrt{|\chi_{(2)}|}(d\theta)_\alpha \wedge (d\phi)_\beta, \quad (128)$$

where $\chi_{(2)}$ is the determinant of the 2-metric χ_{ab}, i.e.

$$\sqrt{|\chi_{(2)}|} = \frac{R^2\sin\theta}{\Omega^2}. \quad (129)$$

Combining all the above relations, for the magnetic charge $\mathrm{Q}^M(T, R)$ associated with a ball of radius R and centered at the origin on a constant T hypersurface we get

$$\begin{aligned} \mathrm{Q}^M(T, R) &= \int_{-\pi}^{\pi}\int_0^{2\pi} \nu^R B_R \sqrt{|\chi_{(2)}|}\, d\theta d\phi \\ &= \int_{-\pi}^{\pi}\int_0^{2\pi} \frac{H(1-w^2)}{gH_0}\sin\theta d\theta d\phi \\ &= \frac{4\pi}{g}\frac{H}{H_0}(1-w^2). \end{aligned} \quad (130)$$

The total magnetic charge Q^M, associated with the entire constant T hyperboloidal hypersurface, can now be given as

$$\mathrm{Q}^M = \mathrm{Q}^M(T, R = 1), \quad (131)$$

which, by virtue of (130) and since w tends to zero exponentially, while H/H_0 tends to one as $R \to 1$, takes the

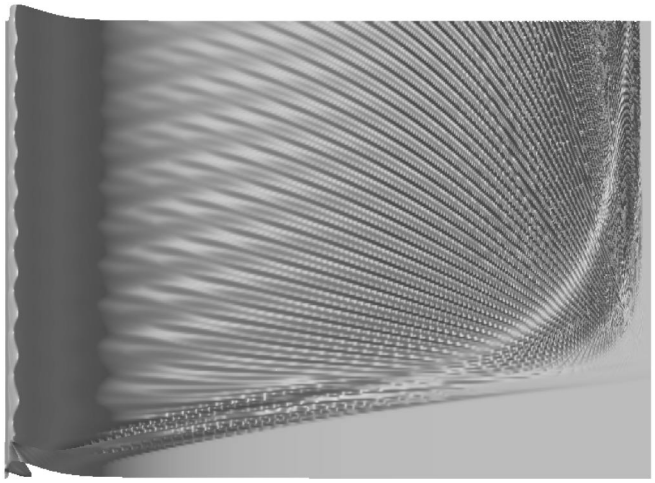

FIG. 39. The space and time dependence of $\tilde{\rho}^M$, the magnetic charge density associated with the shells of radius R, for initial data with amplitude $c = 70$, for the space and time intervals $0 \le R \le 1$ and $0 \le T \le 4.237\,288\,135$. It is transparent that, even though considerably large energy transports occur during the dynamical part, the magnetic charge remains concentrated to the central region throughout the entire evolution. Moreover, an intensive inward pointing current can also be observed in the distant region which quickly returns the lost magnetic charge to the center. Accordingly, the amplitude of the oscillations is decreasing very rapidly there.

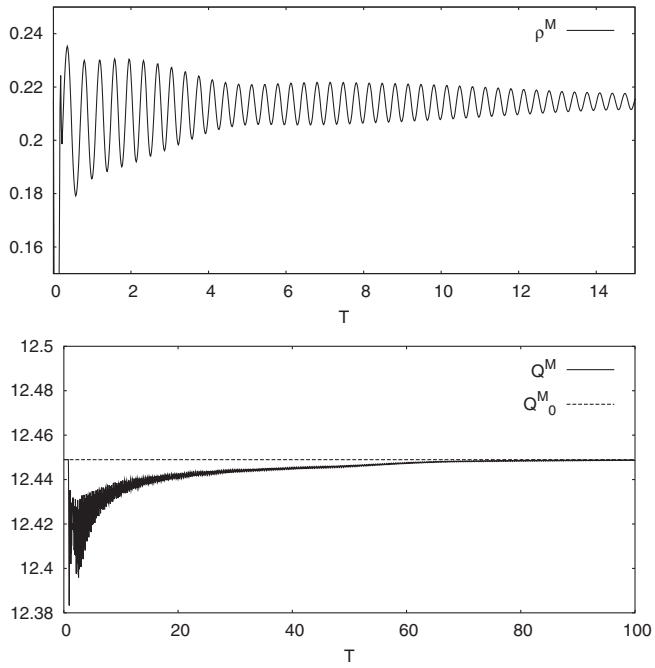

FIG. 40. Upper graph: time dependence of the magnetic charge density ρ^M at the constant R line with $R = 0.067\,797$ ($r = 2.7244$). Lower graph: time dependence of the magnetic charge contained by the ball of radius $R = 0.830\,51$ ($r = 107.07$), centered at the origin. Here Q_0^M denotes the value of the magnetic charge contained by the same ball before the arrival of the exciting pulse. Notice that Q_0^M is, in fact, the value of the magnetic charge contained by the same ball in case of the static monopole.

value

$$\mathrm{Q}^M = \frac{4\pi}{g}. \tag{132}$$

Accordingly, the total magnetic charge Q^M is a time-independent quantity so that its value coincides with the value of the topological charge of the magnetic monopole. Notice also that by virtue of (122) by exciting the initially static BPS monopole by making use only of a nonzero time derivative of the Yang-Mills variable no magnetic charge density, and hence, in accordance with the above conclusion, no magnetic charge is added to the system.

In Fig. 39 the spacetime plot of $\tilde{\rho}^M$, the magnetic charge density associated with the shells of radius R, relevant for the intermediate initial pulse with amplitude $c = 70$, is shown. This quantity $\tilde{\rho}^M$ is defined analogously to those used previously. Accordingly, on any $T = \text{const}$ hypersurface the integral $\int_0^R \tilde{\rho}^M dR$ is supposed to give the magnetic charge contained by the ball of radius R, and as it can be checked easily, $\tilde{\rho}^M = \int_{-\pi}^{\pi}\int_0^{2\pi} \rho^M \sqrt{|h^{(t)}|}\, d\theta d\phi$ or, even more directly, $\tilde{\rho}^M = 4\pi\Omega^3/R^2 \cdot \rho^M = 4\pi/(gH_0) \cdot \partial_R(H[1 - w^2])$. In accordance with the facts that w and H both tend to their asymptotic values, i.e. to zero and one, respectively, very rapidly, even in case of dynamical situations a significant part of the total magnetic charge remains in a small size central region.

This conclusion is also supported by the lower graph of Fig. 40 where the time dependence of $Q^M(T, R)$, the magnetic charge contained by the ball of radius $R = 0.830\,51$ ($r = 107.07$) centered at the origin, is shown. Initially the value is constant until the arrival of the exciting pulse which sweeps out a small fragment of the magnetic charge. Nevertheless, the missing charge returns very rapidly according to the two phase power law scheme indicated by the graph at the bottom.

VIII. FINAL REMARKS

This paper provides a detailed presentation of the analytic and numerical investigations of the time evolution of highly excited t' Hooft-Polyakov magnetic monopoles. The described methods—applying both the techniques of the conformal compactification and the hyperboloidal initial value problem—are of interest on their own as being applicable to generic nonlinear systems in asymptotically flat spacetimes. We hope that the presented details of our numerical scheme might be useful in developing numerical tools by others.

We considered it to be important to check the accuracy and stability of our numerical method in the case of massless and massive Klein-Gordon fields, for which the field values may be determined by independent analytic methods. It was found—see Sec. VI for the associated details—that our code does possess the expected fourth order convergence. Moreover, it is accurate and stable enough to provide the precise field values even for very long term time evolutions.

Then by applying our code to the study of excited magnetic monopoles, it was found to be a powerful tool which is capable to describe the evolution even for highly excited nonlinear systems. In the monitoring of the evolution, we gave special attention to the validity of energy conservation. Since the magnetic monopole is known to be stable, highly excited monopoles should settle down to a breathing state which is known to be a characteristic feature even of slightly perturbed monopoles [5,16]. Our numerical findings, as they are presented in detail in Sec. VII C 2, quantitatively support these expectations.

One of the interesting features of the time evolution of magnetic monopoles is the formation of expanding high frequency shells of oscillations of the massive Yang-Mills field. These are traveling with a speed less than the speed of light towards infinity, carrying and storing a certain part of the energy of the initial pulse. Some other part of the energy is radiated towards null infinity by the massless Higgs field. It was found that except for very large exciting pulses the radiated energy is closely proportional to the energy stored in the high frequency shells of oscillations.

The investigation of the time dependence of the oscillation frequency of the breathing state at the center showed an unexpected similarity in both the features of the graphs and the power of the time decay. The frequency in the central region is getting larger and larger, approaching the upper limit determined by the mass of the system.

The investigated Yang-Mills–Higgs monopole can be endowed with magnetic charge density. The time evolution of the this quantity also shows that the exciting pulse drags with itself some part of the original static monopole. The missing energy and magnetic charge, due to the stability of the monopole, gradually get back to the central region, where the monopole is oscillating forever with a slowly decaying amplitude.

ACKNOWLEDGMENTS

This research was supported in part by the OTKA Grants No. T034337, No. NI68228, No. K67942 and the NATO Grant No. PST.CLG.978726.

APPENDIX A

The regularity properties (17)–(19) of the field variables at the origin can be justified by substituting the expansions

$$w(t, r) = \sum_{k=0}^{n} \frac{1}{k!} w_k(t) r^k + \mathcal{O}_w(r^{n+1}), \tag{A1}$$

$$H(t, r) = \sum_{k=0}^{n} \frac{1}{k!} H_k(t) r^k + \mathcal{O}_H(r^{n+1}) \tag{A2}$$

into the field equations and requiring that the coefficients of the various powers of r vanish identically. The yielded

restrictions are

$$w_0(t) = 1, \tag{A3}$$

$$\partial_r^k w|_{r=0} = w_k(t) = 0, \tag{A4}$$

for k being odd, and

$$H_0(t) = 0, \tag{A5}$$

$$\partial_r^k H|_{r=0} = H_k(t) = 0, \tag{A6}$$

for k being even. It also follows from these relations, along with (A1) and (A2), that at the origin the time derivatives $\partial_t w$ and $\partial_t H$ have to vanish throughout the evolution.

Note that part of these restrictions can also be deduced in a different way. In particular, by substituting (A1) and (A2) into the tetrad components of the energy-momentum tensor we immediately get that these components cannot be finite at the origin unless the relations

$$w_0(t) = 1, \tag{A7}$$

$$w_1(t) = 0, \tag{A8}$$

$$H_0(t) = 0 \tag{A9}$$

are satisfied.

To get the regularity result at future null infinity we need to transform the field Eqs. (15) and (16) into a form suitable to study the asymptotic behavior of the fields at $\mathscr{I}^+$. Therefore, instead of the standard coordinates (t, r, θ, ϕ) we apply coordinates (u, x, θ, ϕ) based on outgoing null geodesic congruences determined by the relations

$$u = t - r \quad \text{and} \quad x = \frac{1}{r}. \tag{A10}$$

In this frame future null infinity is represented by the $x = 0$ hypersurface; moreover, the field Eqs. (15) and (16) read as

$$x^2\partial_x^2 w + 2x\partial_x w + 2\partial_x\partial_u w = w\left[(w^2 - 1) + \frac{g^2H^2}{x^2}\right], \tag{A11}$$

$$x^3\partial_x^2 H - 2\partial_u H + 2x\partial_u\partial_x H = xH\left[2w^2 + \frac{\lambda}{2x^2}(H^2 - H_0^2)\right]. \tag{A12}$$

Consider now the expansions

$$w = \sum_{k=0}^{n} \frac{1}{k!} w_k(u)x^k + \mathcal{O}_w(x^{n+1}), \tag{A13}$$

$$H = \sum_{k=0}^{n} \frac{1}{k!} H_k(u)x^k + \mathcal{O}_H(x^{n+1}), \tag{A14}$$

which are valid in a neighborhood of $x = 0$ whenever w and H are at least C^n functions through $\mathscr{I}^+$, where the notations $w_k(u) = \partial_x^k w(u, x)|_{x=0}$ and $H_k(u) = \partial_x^k H(u, x)|_{x=0}$ have been used. By substituting these expansions into the field Eqs. (A11) and (A12) we get the following: Whenever $\lambda \neq 0$

$$w(u) = 0, \tag{A15}$$

$$H(u) = H_0, \tag{A16}$$

$$\partial_x^k w = w_k(u) = 0, \tag{A17}$$

$$\partial_x^k H = H_k(u) = 0 \tag{A18}$$

for all $0 < k < n$, i.e., in accordance with the results of Winicour [26], both of the fields decay faster than x^n to their limit values at $\mathscr{I}^+$. On the other hand, whenever $\lambda = 0$ and H_∞ is nonzero, only the vanishing of the x derivatives of w (up to the order of n) is guaranteed while we get $\partial_u H = 0$, i.e. H_∞ is independent of u, there is no restriction for $\partial_u\partial_x H$, and finally, $\partial_u(\partial_x^k H) = 0$ for $2 \leq k < n$ provided that singular behavior of the field at future (or past) timelike infinity is excluded. Note that the missing of a restriction on $\partial_u\partial_x H$ is in accordance with the following physical picture. The term $\partial_u\partial_x H$ appears in the energy current expression; thereby, whenever $\lambda = 0$ the massless Higgs fields do transport energy to $\mathscr{I}^+$. The extent of this energy transport is restricted only by the initial data and the field equation.

Interesting subcases occur (which would deserve further investigations) whenever

(i) $\lambda = 0$ and $H_\infty = 0$,
(ii) $\lambda \neq 0$ and $H_0 \neq 0$ but $H_\infty = 0$, and
(iii) $\lambda \neq 0$ and $H_0 = 0$.

Then either or both of the fields are massless and there is no restriction on the behavior of the actual massless field or fields at $\mathscr{I}^+$.

The above considerations show that a YMH system satisfying reasonable regularity assumptions at $\mathscr{I}^+$ cannot radiate energy to future null infinity unless either $\lambda = 0$, $H_0 = 0$, or $H_\infty = 0$.

APPENDIX B

This appendix lists expressions we applied to represent various numerical R derivatives in miscellaneous stencils. The expressions below always refer to an arbitrary function f on the lth time slice.

The first order R derivative relevant for a symmetric fourth order stencil reads

$$(\partial_R f)_i^l \to \frac{1}{12\Delta R}(-f_{i+2}^l + 8f_{i+1}^l - 8f_{i-1}^l + f_{i-2}^l). \tag{B1}$$

The sixth order R derivative relevant for a symmetric sixth order stencil was approximated as

$$(\partial_R^6 f)_i^l \to \frac{1}{(\Delta R)^6}(f_{i+3}^l - 6f_{i+2}^l + 15f_{i+1}^l - 20f_i^l + 15f_{i-1}^l - 6f_{i-2}^l + f_{i-3}^l). \quad \text{(B2)}$$

We also used a numerical adaptation called one-sided derivatives in analytic investigations. The relevant first order "left-sided derivatives" are approximated in our fourth order stencil as

$$(\partial_R f)_{I_{\max}}^l \to \frac{1}{12\Delta R}(3f_{I_{\max}-4}^l - 16f_{I_{\max}-3}^l + 36f_{I_{\max}-2}^l - 48f_{I_{\max}-1}^l + 25f_{I_{\max}}^l) \quad \text{(B3)}$$

at $i = I_{\max}$ and as

$$(\partial_R f)_{I_{\max}-1}^l \to \frac{1}{12\Delta R}(-f_{I_{\max}-4}^l + 6f_{I_{\max}-3}^l - 18f_{I_{\max}-2}^l + 10f_{I_{\max}-1}^l + 3f_{I_{\max}}^l) \quad \text{(B4)}$$

at $i = I_{\max} - 1$.

The analogous sixth order left-sided derivatives in a sixth order stencil at the spatial grid points with indices $I_{\max}$, $I_{\max} - 1$, and $I_{\max} - 3$ do not differ from each other. They are simply yielded by the substitution of $i = I_{\max} - 3$ into (B2).

[1] N. S. Manton and P. Sutcliffe, *Topological Solitons* (Cambridge University Press, Cambridge, England, 2004).
[2] V. Rubakov, *Classical Theory of Gauge Fields* (Princeton University Press, Princeton, NJ, 2002).
[3] G. Fodor, P. Forgács, P. Grandclément, and I. Rácz, Phys. Rev. D **74**, 124003 (2006).
[4] G. Fodor and I. Rácz, Phys. Rev. D **68**, 044022 (2003).
[5] G. Fodor and I. Rácz, Phys. Rev. Lett. **92**, 151801 (2004).
[6] G. Fodor and I. Rácz, in *Proceedings of the Seventh Hungarian Relativity Workshop, Sárospatak, 2003*, edited by I. Rácz (Akadémiai Kiadó, Budapest, 2004), pp. 205–217.
[7] P. Csizmadia, Int. J. Mod. Phys. D **15**, 107 (2006).
[8] P. Csizmadia, Classical Quantum Gravity **24**, S369 (2007).
[9] P. Csizmadia, G. Fodor, I. Rácz, and Á. Rusznyák, The Time Evolution of Generic Spherically Symmetric Magnetic Monopoles (unpublished).
[10] P. Csizmadia, G. Fodor, and I. Rácz, Numerical Investigation of Highly Excited Magnetic Monopoles in $SU(2)$ Yang-Mills–Higgs Theory II. (unpublished).
[11] B. Gustafsson, H.-O. Kreiss, and J. Oliger, *Time Dependent Problems and Difference Methods*, Pure and Applied Mathematics (Wiley, New York, 1995).
[12] J. Hansen, A. Khokhlov, and I. Novikov, Int. J. Mod. Phys. D **13**, 961 (2004).
[13] R. Penrose, Proc. R. Soc. A **284**, 159 (1965).
[14] A. M. Polyakov, JETP Lett. **20**, 194 (1974).
[15] E. B. Bogomolny, Sov. J. Nucl. Phys. **24**, 449 (1976).
[16] P. Forgács and M. S. Volkov, Phys. Rev. Lett. **92**, 151802 (2004).
[17] E. Farhi, N. Graham, V. Khemani, R. Markov, and R. Rosales, Phys. Rev. D **72**, 101701 (2005).
[18] M. Gleiser, Int. J. Mod. Phys. D **16**, 219 (2007).
[19] M. Gleiser and J. Thorarinson, Phys. Rev. D **76**, 041701 (2007).
[20] N. Graham, Phys. Rev. Lett. **98**, 101801 (2007).
[21] N. Graham, Phys. Rev. D **76**, 085017 (2007).
[22] P. M. Saffin and A. Tranberg, J. High Energy Phys. 01 (2007) 030.
[23] G. t' Hooft, Nucl. Phys. **B79**, 276 (1974).
[24] P. Goddard and D. I. Olive, Rep. Prog. Phys. **41**, 1357 (1978).
[25] K. Huang, *Quarks, Leptons and Gauge Fields* (World Scientific, Singapore, 1992).
[26] J. Winicour, J. Math. Phys. (N.Y.) **29**, 2117 (1988).
[27] J. Burzlaff and N. O'Murchadha, Commun. Math. Phys. **105**, 85 (1986).
[28] D. M. Eardley and V. Moncrief, Commun. Math. Phys. **83**, 171 (1982).
[29] D. M. Eardley and V. Moncrief, Commun. Math. Phys. **83**, 193 (1982).
[30] V. Moncrief, in *Seminar on New Results in Nonlinear Partial Differential Equations*, edited by A. J. Tromba (Friedrick Vieweg & Son, Bonn, 1987), pp. 91–100.
[31] M. K. Prasad and C. M. Sommerfield, Phys. Rev. Lett. **35**, 760 (1975).
[32] J. Baacke, Z. Phys. C **53**, 399 (1992).
[33] V. Moncrief, *Proceedings of the Workshop on Mathematical Issues in Numerical Relativity, Santa Barbara, 2000.*
[34] S. Husa, in *Proceedings of the 2001 Spanish Relativity Meeting*, Lecture Notes in Physics series, edited by L. Fernandez and L. Gonzalez (Springer, New York, 2003) [Lect. Notes Phys. **617**, 159 (2003)].
[35] A. Zenginoglu and S. Husa, arXiv:gr-qc/0612161.
[36] R. Courant and D. Hilbert, Methods of Mathematical Physics (Interscience, New York, 1962), Vol. II.
[37] B. Julia and A. Zee, Phys. Rev. D **11**, 2227 (1975).